First assessment of Aeolus SCA particle backscatter coefficient retrievals in the Eastern Mediterranean

Antonis Gkikas[1,9], Anna Gialitaki[1,5,6], Ioannis Binietoglou[1], Eleni Marinou[1], Maria Tsichla[1], Nikolaos Siomos[1], Peristera Paschou[1,5], Anna Kampouri[1,7], Kalliopi Artemis Voudouri[1,5], Emmanouil Proestakis[1], Maria Mylonaki[2], Christina-Anna Papanikolaou[2], Konstantinos Michailidis[5], Holger Baars[3], Anne Grete Straume[4], Dimitris Balis[5], Alexandros Papayannis[2], Tomasso Parrinello[8] and Vassilis Amiridis[1]

[1]Institute for Astronomy, Astrophysics, Space Applications and Remote Sensing, National Observatory of Athens, Athens, Greece

[2]Laser Remote Sensing Unit, Department of Physics, National and Technical University of Athens, Athens, Greece

[3]Leibniz-Institut für Troposphärenforschung e.V., Leipzig, Germany

[4]European Space Agency (ESA/ESTEC), Noordwijk, Netherlands

[5]Laboratory of Atmospheric Physics, Aristotle University of Thessaloniki, Thessaloniki, Greece

[6]Department of Physics and Astronomy, University of Leicester, Leicester, United Kingdom

[7]Department of Meteorology and Climatology, School of Geology, Aristotle University of Thessaloniki, 54124 Thessaloniki, Greece

[8]European Space Agency (ESA/ESRIN), Frascati, Italy

[9]Research Centre for Atmospheric Physics and Climatology, Academy of Athens, 10680 Athens, Greece

Corresponding author: Antonis Gkikas (agkikas@noa.gr)

Abstract

Since 2018, the Aeolus satellite of the European Space Agency (ESA) acquires wind HLOS (horizontal line-of-sight) profiles throughout the troposphere and up to the lower stratosphere, filling a critical gap of the Global Observing System (GOS). Aeolus, carrying ALADIN (Atmospheric LAser Doppler INstrument), the first UV HSRL (High Spectral Resolution Lidar) Doppler lidar ever placed in space, provides also vertically resolved optical properties of particulates (aerosols, clouds). The present study focuses on the assessment of Aeolus L2A particulate backscatter coefficient (baseline 2A11), retrieved by the Standard Correct Algorithm (SCA), in the Eastern Mediterranean, a region hosting a variety of aerosol species. Ground-based retrievals acquired by lidar instruments operating in Athens (central Greece), Thessaloniki (north Greece) and Antikythera (southwest Greece) serve as reference. All lidar stations provide routine measurements to the PANACEA (PANhellenic infrastructure for Atmospheric Composition and climatE chAnge) network. A set of ancillary data including sunphotometric observations (AERONET), reanalysis products (CAMS, MERRA-2),

satellite observations (MSG-SEVIRI, MODIS-Aqua) and backward trajectories modelling (FLEXPART) are utilized towards an optimum characterization of the probed atmospheric conditions under the absence of a classification scheme in Aeolus SCA profiles. First, emphasis is given on the assessment of Aeolus SCA backscatter coefficient under specific aerosol scenarios over the Antikythera island. Due to the misdetection of the cross-polar component of the backscattered lidar signal, Aeolus underestimates the aerosol backscatter coefficient by up to 33% when non-spherical mineral particles are recorded (10th July 2019). A good performance is revealed on 3rd July 2019, when horizontally homogeneous loads of fine spherical particles are confined below 4 km. For other two cases (8th July 2020, 5th August 2020), due to noise issues, the SCA performance degrades in terms of depicting the stratification of aerosol layers composed of particles of different origin. According to the statistical assessment analysis of 43 identified cases, it is revealed a poor-to-moderate performance for the unfiltered (aerosols plus clouds) SCA profiles which improves substantially when cloud contaminated profiles are excluded from the collocated sample. This improvement is evident at both Aeolus vertical scales (regular, 24 bins and mid-bin, 23 bins) and it is justified by the drastic reduction of the bias (from 0.45 $Mm^{-1}sr^{-1}$ to 0.27 $Mm^{-1}sr^{-1}$ for SCA and from 0.69 $Mm^{-1}sr^{-1}$ to 0.37 $Mm^{-1}sr^{-1}$ for SCA mid-bin) and root-mean-square-error (from 2.00 $Mm^{-1}sr^{-1}$ to 1.65 $Mm^{-1}sr^{-1}$ for SCA and from 1.88 $Mm^{-1}sr^{-1}$ to 1.00 $Mm^{-1}sr^{-1}$ for SCA mid-bin) scores. In vertical, the SCA performance degrades at the lowermost bins due to either the contamination from surface signals or the increased noise levels for the aerosol retrievals. Among the three PANACEA stations, the best agreement is found at the remote site of Antikythera with respect to the urban sites of Athens and Thessaloniki. Finally, all key Cal/Val aspects necessary for future relevant studies, the recommendations for a possible Aeolus follow-on mission and an overview of the ongoing related activities are thoroughly discussed.

1. Introduction

Atmospheric aerosols constitute a critical component of the Earth system by acting as a major climatic driver (Charlson et al., 1992; Boucher et al., 2013; Li et al., 2022) whereas upon deposition they can affect terrestrial (Okin et al., 2004) and marine ecosystems (Jickells et al., 2005; Li et al., 2018). It is also well documented that they affect several anthropogenic activities with concomitant economic impacts (Middleton et al., 2018; Kosmopoulos et al., 2018). In addition, aerosols accumulation at large concentrations cause an air quality degradation (Kanakidou et al., 2011) with adverse health effects (Pöschl, 2005; Lelieveld et al., 2015) increasing the mortality rates (Health Effects Institute, 2019; Pye et al., 2021). Therefore, their multifaceted role in multidisciplinary research fields highlights the growing scientific concern in understanding and describing the

Deleted: L2A

Deleted: Aeolus

Deleted: downgrades

Deleted: for

Deleted: Aeolus

Deleted: Aeolus

Deleted: downgrades

emission, removal, and transport mechanisms governing airborne particles' life cycle. Due to their pronounced heterogeneity, aerosol burden exhibits a remarkable spatiotemporal variability thus imposing deficiencies in depicting adequately its features and constraints towards a robust assessment of the induced impacts.

Passive satellite sensors, providing columnar retrievals of aerosol optical depth (AOD), have been able to reproduce adequately aerosol loads across various spatiotemporal scales. This has been justified via the assessment of AOD versus corresponding sun-photometric measurements (e.g., Wei et al., 2019). Nevertheless, the main drawback arises from the sensors' inability to provide information in vertical. Therefore, this deficiency hampers a reliable quantification of the suspended particles' load within the planetary boundary layer (PBL), related to health impacts. Moreover, it is not feasible to depict the three-dimensional structure of transported loads in the free troposphere, linked to aerosol-cloud-radiation interactions and associated impacts on atmospheric dynamics (Pérez et al., 2006; Gkikas et al., 2018; Haywood et al., 2021). Likewise, passive aerosol observations are not suitable for monitoring stratospheric long-lived plumes that affect aerosol-chemistry interactions and perturb the radiation fields (Solomon et al., 2022). On the contrary, ground-based lidars, relying on active remote sensing techniques, obtain vertical profiles of aerosol optical properties at high vertical and temporal resolution, through multi-wavelength and polarization measurements. Such observations are performed either at networks distributed across Europe (EARLINET; Papalardo et al., 2014; PollyNET; Baars et al., 2016; Engelmann et al., 2016), United States (MPLNET; Campbell et al., 2002), Asia (AD-NET; Sugimoto et al., 2014) and South America (LALINET; Guerrero-Rascado et al., 2016), or at dedicated experimental campaigns (Ansmann et al., 2011; Weinzierl et al., 2016) or even at open seas (Bohlmann et al., 2018). The reproduction of aerosols' vertical structure at global (Liu et al., 2008) and regional (Marinou et al., 2017; Proestakis et al., 2018) scales has been realized through the utilization of measurements acquired by the Cloud-Aerosol Lidar and Infrared Pathfinder Satellite Observation (CALIOP; Winker et al., 2009) and the Cloud-Aerosol Transport System (CATS; McGill et al., 2015; Lee et al., 2019) mounted on the CALIPSO (Cloud-Aerosol Lidar and Infrared Pathfinder Satellite Observation) satellite and the International Space Station (ISS), respectively.

On 22nd August 2018, the European Space Agency (ESA) launched its Earth Explorer wind mission, Aeolus, which was a major step forward for Earth Observations (EO) and atmospheric sciences. The Aeolus satellite carries ALADIN (Atmospheric LAser Doppler INstrument), the first space-based high spectral resolution (HSRL) Doppler wind lidar worldwide. ALADIN emits a linear polarized beam which after going through a quarter-wave plate is transmitted with a circular polarization (at 355 nm) and receives the co-polarized backscatter from molecules and

particles/hydrometeors in two separate channels (Ansmann et al., 2007; Flamant et al., 2008). The main mission product is profiles of the horizontally projected line-of-sight winds, and spin-off products are the backscatter and extinction coefficient profiles from particles and hydrometeors. The key scientific objective of Aeolus is to improve numerical weather forecasts and our understanding of atmospheric dynamics and their impacts on climate (Stoffelen et al., 2005; Isaksen and Rennie, 2019; Rennie and Isaksen, 2019). After about 1.5 years of instrument and algorithm improvements, the Aeolus L2B wind product was of such good quality (e.g., Witschas et al., 2020; Lux et al., 2020; Martin et al., 2021) that the European Centre for Medium Range Forecasts (ECMWF) could start operational assimilation (January 2020). In May 2020, three further European weather forecast institutes (DWD, Météo-France and the UK MetOffice) started the operational assimilation of Aeolus winds. All meteorological institutes reported that Aeolus winds had significant positive impact on the short and medium term forecasts. The most beneficial impact is found in remote areas (Tropics, S. Hemisphere, polar regions) less covered by other direct wind observations (e.g. ECMWF 2020; Rennie et al., 2021).

A series of errors induced by the instrument, by the retrieval algorithm, or by the type of scatterers probed by ALADIN can affect the product quality. It is therefore necessary to perform extensive calibration and validation (Cal/Val) studies utilizing independent reference measurements (e.g. ground-based, aircraft). This task has been performed by the Aeolus Cal/Val community, responding to the Aeolus Announcement of Opportunity to perform product calibration and validation. Such critical tasks are prerequisites to the acceptance of the Mission as "fit for purpose" as it is underlined in the Aeolus Implementation Cal/Val Plan. In contrast to Aeolus wind retrievals, a limited number of studies are focused on the quality of the L2A SCA optical properties. Abril-Gago et al. (2022) performed a statistical validation versus ground-based observations from three Iberian ACTRIS/EARLINET lidar stations affected mainly by dust and continental/anthropogenic aerosols. In their Cal/Val study, they processed AERONET optical properties related to particles' size and nature along with HYSPLIT air-mass backtrajectories towards characterizing the prevailing aerosol conditions. Baars et al. (2021) reported an excellent agreement between SCA and Polly^{XT} particle backscatter profiles and adequate agreement of extinction and lidar ratio profiles, between 4 and 12 km, for a case of long-range transport of wildfire smoke particles from California to Leipzig (Germany).

Here we focus on the comparison of Aeolus SCA particle backscatter coefficient profiles against ground-based profile observations acquired at three lidar stations (Antikythera, Athens, Thessaloniki) contributing to the Greek National Research Infrastructure (RI) PANACEA, an

ACTRIS component (https://www.actris.eu). All stations are located in the Eastern Mediterranean, a crossroad of air masses (Lelieveld et al., 2002) carrying particles of different nature. The broader Greek area encompasses a variety of aerosol species consisting of: (i) pollutants from industrialized European regions (Gerasopoulos et al., 2003; 2009), (ii) dust aerosols from the nearby deserts (Balis et al., 2004; Papayannis et al., 2005; Gkikas et al., 2016, Marinou et al., 2017), (iii) anthropogenic aerosols from urban areas and megacities (Kanakidou et al., 2011), (iv) biomass burning particles originating in the eastern Europe and the Black Sea (Amiridis et al., 2009; 2010; 2012), (v) smoke aerosols subjected to transport at planetary scale (Baars et al., 2019; Gialitaki et al., 2020), (vi) sea-salt particles produced by bursting bubbles during whitecap formation attributed to wind-wave interactions (e.g. Varlas et al., 2021), (vii) biogenic particles such as airborne fungi and pollen grains (Richardson et al., 2019) and (viii) volcanic ash mixed with sulfate aerosols ejected at high altitudes from explosive Etna eruptions (Zerefos et al., 2006, Kampouri et al., 2021).

The manuscript is structured as follows. In Section 2, a brief overview of the Aeolus satellite and the ALADIN instrument is given. The key elements of the Standard Correct Algorithm (SCA) are summarized in Section 3. The technical information of the ground-based lidars as well as the description of aerosols' regime, in the surrounding area of the PANACEA stations, are presented in Section 4. The collocation criteria between ground-based and spaceborne profiles are described in Section 5. The assessment of Aeolus SCA product under various aerosol scenarios and for the whole collocated sample are discussed in Section 6. The Cal/Val aspects, the recommendations for future relevant studies and the necessary upgrades on ALADIN observational capabilities and Aeolus L2A data content are highlighted in Section 7. Finally, the main findings and the conclusions are drawn in Section 8.

2. AEOLUS - ALADIN

A brief description of Aeolus' orbital features, ALADIN's observational geometry and its measurement configuration is given in the current section. This short introduction serves as the starting point for the reader to be familiar with Aeolus' nomenclature. Further details and a more comprehensive overview of the Aeolus satellite mission can be found at ESA technical reports (ESA, 1999; 2008; 2016) and at recently published studies (e.g., Lux et al., 2020; Witschas et al., 2022; Lux et al., 2022).

ESA's Aeolus satellite, named after the 'keeper of winds' according to the Greek mythology (Ingmann and Straume, 2016), flies in a polar sun-synchronous orbit circling the Earth at an altitude of 320 km with a repeat cycle of 7 days (Kanitz et al., 2019a; Straume et al., 2019). The orbital plane forms an angle of 97° with the equatorial plane, the ground track velocity is about 7.7 km/sec and a complete circle around the Earth takes about 90 minutes for each orbit (Lux et al., 2020; Witschas et al., 2020; Straume et al., 2020). Aeolus is flying over the terminator between day and night (dawn/dusk orbits), with its telescope pointing to the right of the flight direction (aiming into the night hemisphere) for minimizing the solar background illumination (Kanitz et al., 2019).

ALADIN, the single payload on the Aeolus satellite platform, is an HSRL (Shipley et al., 1983) equipped with a Nd-YAG laser that emits short laser pulses (~40 to 70 mJ, Witchas et al., 2020) of a circular polarized light at ~355 nm with a 50.5 Hz repetition frequency. The photons that are backscattered from molecules and particulates (aerosols, cloud droplets and ice crystals) at atmospheric altitudes lower than 30 km are collected by a Cassegrain telescope of 1.5 m diameter. The collected photons are directed to the Mie optical channel (Fizeau interferometer) for the analysis of the Doppler shift induced by particulates while the molecular return signals (Rayleigh) are analyzed in two sequentially coupled Fabry–Pérot interferometers (Witchas et al., 2020).

ALADIN provides wind and particulate vertically resolved retrievals along the Line-Of-Sight (LOS) by pointing the Earth at a slant angle of 35° off-nadir (see Figure 1 in Flament et al., (2021)) which corresponds to an angle of about 37.6° with the Earth surface, due to its curvature. In contrast to CALIOP and CATS, ALADIN can retrieve particulate optical products without requiring an a priori assumption of the lidar ratio (S), which is characterized by a remarkable variability among aerosol types due to its dependency on particles' shape, composition and size distribution (Müller et al., 2007). However, ALADIN only measures the co-polar part of the atmospheric backscatter and at a single wavelength. Therefore, the discrimination between aerosols and clouds and their respective subtypes is challenging.

The instrument detector design allows the sampling of the atmospheric backscatter in 24 vertical bins, with a varying resolution from 0.25 (near surface) to 2 km (upper atmosphere). The laser pulses are integrated on-board the satellite along the flight direction, to yield measurements of ~3 km resolution (integration of ~20 laser pulses). During the on-ground data processing, the measurements are accumulated further to yield an "*observation*" (also called a *Basic Repeat Cycle (BRC)),* which corresponds to a distance of ~90 km. The SCA optical properties are part of the L2A product which will be described in the next section, and are derived by the so-called Standard Correct Algorithm (SCA) (Flament et al., 2021). They are provided at the observation scale (on a horizontal

resolution of ~90 km) and are available through the Aeolus Online Dissemination System (https://aeolus-ds.eo.esa.int)

3. Standard Correct Algorithm (SCA)

In the current Cal/Val study, we are assessing the performance of the Aeolus L2A particulate products derived by the Standard Correct Algorithm (SCA). Here, we are providing a short overview of the SCA whereas its complete description is available in the Algorithm Theoretical Baseline Document (ATBD; Flamant et al., 2021). The SCA product is derived from the measured signals in the Mie and Rayleigh channels, which are dependent on the instrument calibration constants (K_{ray}, K_{mie}), the channel cross-talk coefficients C_1, C_2, C_3 and C_4, the laser pulse energy (E_0) and the contributions from the pure molecular (X) and particulate (Y) signals (see Equations 1 and 2 in Flament et al. (2021)). The latter ones, at each bin, result from the vertical integration of the backscatter (either molecular or particulate) where the squared one-way transmission through the atmosphere is taken into account (see Equations 3 and 4 in Flament et al. (2021)).

The separation of the molecular and particle signals on each channel is imperfect, due to the HSRL instrument design, which makes necessary a cross-talk correction. The channel cross-talk corresponding to the transmission of the Rayleigh-Brillouin spectrum (depending on the temperature, pressure and the Doppler shift) through the Rayleigh and Mie channels is expressed by the calibration coefficients C_1 and C_4, respectively (Flament et al., 2021). The other two coefficients, C_2 and C_3, refer to the transmission of a Mie spectrum (depending on the Doppler shift) through the Mie and Rayleigh channels, respectively. Along with the cross-talk coefficients, the instrument calibration constants (K_{ray}, K_{mie}) (see in Flament et al., 2021) are included in the AUX_CAL files.

Finally, the cross-talk corrected signals, normalized with the range bin thickness and corrected by the range between the satellite and the observed target, are utilized for the retrieval of the vertically resolved backscatter (β) and extinction (α) coefficients. The former, at each bin, is derived by the Y/X ratio multiplied with the molecular backscatter coefficient (see Equations 9 and 10 in Flament et al., 2021) computed from the pressure and temperature ECMWF simulated fields (Collis and Russel, 1976). For the SCA extinction retrievals, derived via an iterative process from top to bottom, the normalized integrated two-way transmission (NITWT) is applied, using measured and simulated pure molecular signals, under the assumption that the particles' extinction at the top-most bin is zero (see equations 11-14 in Flament et al., 2021). This consideration makes the downwards solution of the integral equations quite sensitive to the noise within the topmost bin (at altitudes ~20-25 km), which is used as reference for the normalization, particularly under low SNR conditions due to the low molecular density. This is a challenge frequently faced for the SCA observations due to the weaker

266 measured signals than those of the pre-launch expectations (Reitebuch et al., 2020) as well as to the
267 possible presence of stratospheric aerosols within the top-most range bin or above. In principle, the
268 extinction is retrieved recursively taking into account the attenuation from the overlying bins and by
269 contrasting observed and simulated molecular signals. By differentiating two consecutive bins,
270 unrealistically high positive or negative extinctions can be retrieved (see Fig. 10 in Flament et al.,
271 (2021)) resulting from fluctuations between strong and weak attenuation.

272 In the case of negative extinction values, the SCA algorithm regularizes the solution by
273 resetting to zero (Flament et al., 2021), which can lead to an underestimation of the partial column
274 transmission. In order to compensate the impacts of the aforementioned issues, it has been shown by
275 error propagation calculations (see equations 18 and 19 in Flament et al. (2021)), that averaging two
276 consecutive bins the retrieved extinction becomes more reliable at the expense of the vertical
277 resolution (23 bins; "mid-bin" vertical scale). In contrast to SCA, in the SCA mid-bin negative
278 extinction values can be found since the zero-flooring constraint is not implemented. For consistency
279 reasons, the averaging between two neighboring bins is applied also in the backscatter coefficient
280 thus allowing the derivation of the lidar ratio.

281 The inherent weaknesses of the SCA algorithm have been mitigated in the Maximum
282 Likelihood Estimation (MLE) algorithm (Ehlers et al., 2022). Its main principle relies on the
283 exploitation of all available information and the definition of constraints on the positivity of the
284 retrieved optical properties and on the expected range of the lidar ratio. Under these restrictions, the
285 particle extinction is derived when the particle backscatter is available and vice versa. According to
286 the evaluation versus ground-based observations and SCA end-to-end simulated optical products, it
287 is revealed a remarkable improvement (up to one order) on the precision of the extinction and the
288 lidar ratio due to effective noise dampening. Moreover, there is also a beneficial impact on the co-
289 polar backscatter coefficient. Another new algorithm that outperforms SCA is the AEL algorithm
290 (adjusted from the EarthCARE-ATLID algorithms) providing a feature mask (AEL-FM) at the
291 highest available resolution and aerosol/clouds extinction and lidar ratios via a multi-scale optimal
292 estimation method (AEL-PRO). Both MLE and AEL retrievals have been released at a more recent
293 baseline (2A14) than those used in the current study (2A11) and for this reason are omitted from our
294 Cal/Val analysis.

295

296 **4. Ground-based lidars (PANACEA)**

297 The ground-based observational datasets used herein, are taken from stations contributing to
298 the PANhellenic infrastructure for Atmospheric Composition and climatE chAnge (PANACEA)
299 initiative. Within PANACEA, different measurement techniques and sensors are utilized in a

synergistic way for monitoring the atmospheric composition and climate change related parameters in Greece.

The locations of the stations providing routine measurements to the PANACEA network are shown in Figure 1-i. For the assessment analysis of Aeolus SCA optical properties, we utilize available measurements from PANACEA stations, namely Antikythera (ANT), Athens (ATH) and Thessaloniki (THE), equipped with multiwavelength polarization lidar systems. All stations comply with the quality-assurance criteria established within EARLINET (e.g. see Freudenthaler et al., 2016) so as to assure the provision of high-quality aerosol related products. Consequently, the derived datasets can be considered for any validation purpose. To ensure the homogeneity and the consistency of the optical property profiles derived from the adverse lidar systems operating at each station, the Single Calculus Chain algorithm (SCC; D' Amico et al., 2016; Mattis et al., 2016) was used; an automatic processing chain for lidar data, developed within EARLINET. All systems employ multiple detectors, operating either in the photon-counting or analog mode. Herein elastically and inelastically backscattered signals at 355 and 387 nm, were used to evaluate Aeolus products. The optical property profiles were derived using the Raman and Klett-Fernald-Sassano inversion methods (Ansmann et al. 1992; Fernald, 1984; Klett, 1981; Sasano and Nakame, 1984) during night-time and daytime measurements respectively.

4.1 Antikythera

Regular lidar measurements have been performed at the PANGEA observatory (PANhellenic GEophysical observatory of Antikythera; lat=35.86° N, lon=23.31° E, alt=193 m asl.) contributing to this study. The lidar system deployed at PANGEA is operated by the National Observatory of Athens (NOA). It is a Polly[XT] (Engelmann et al., 2016) multi-wavelength Polarization-Raman-Water vapor lidar, designed for unattended, continuous operation. Polly [XT] deploys an Nd:YAG laser which emits linearly polarized light at 355, 532 and 1064 nm. The radiation elastically and inelastically backscattered from aerosol, cloud particles, nitrogen (at 387 and 607 nm) and water vapor (at 407 nm) molecules, is collected using a near-range (spherical mirror of 50 mm diameter, focal length f=250 mm and 2.2 mrad field of view (FOV)) and a far-range receiver (Newtonian telescope with a 300 mm diameter primary mirror, f=900 m and 1 mrad FOV) at a raw vertical resolution of 7.5m. The combined use of the near-range and far-range receivers allows for the retrieval of the aerosol optical properties from 500 m up to ~12-14 km above the ground. A detailed description of the technical characteristics of Polly[XT] can be found in Engelmann et al. (2016).

4.2 Athens

336   The Laser Remote Sensing Unit of the National and Technical University of Athens, Greece
337   (LRSU; NTUA; lat=37.96° N, lon=23.78° E, alt=200 m asl.), is part of the EARLINET since May
338   2000. Currently, the Athens lidar station performs simultaneous measurements with two different
339   lidar systems, EOLE and DEPOLE. The EOLE lidar is an advanced 6-wavelength elastic
340   backscatter/Raman lidar system able to provide the aerosol backscatter coefficient at 355, 532 and
341   1064 nm, the aerosol extinction coefficient at 355 and 532 nm and water vapor mixing ratio profiles
342   in the troposphere. EOLE is based on a pulsed Nd:YAG laser system and a 300 mm diameter
343   receiving Cassegrain telescope (f=600 mm, FOV =1.5 mrad) which collects all elastically
344   backscattered lidar signals (355-532-1064 nm), as well as generated by the vibrational Raman effect
345   (by atmospheric N_2 at 387-607 nm and by H_2O at 407 nm). The full overlap (i.e. the altitude from
346   which upwards the whole lidar beam is within the telescope FOV) of EOLE is reached at,
347   approximately, 812 m a.s.l.. EOLE has been validated within EARLINET at hardware level by two
348   intercomparison campaigns (Matthias et al., 2004), in order to fulfill the standardized criteria.

349   The DEPOLE lidar is a depolarization lidar, able to provide profiles of the aerosol backscatter
350   coefficient and the linear particle/volume depolarization ratio at 355 nm. DEPOLE is based on a
351   pulsed Nd:YAG laser system which emits linearly polarized light at 355 nm. The elastically
352   backscattered lidar signals at 355 nm are collected by a 200 m diameter Dall-Kirkham/Cassegrain
353   telescope (f=600 mm, FOV=3.13 mrad) and the full overlap is reached at, approximately, 500 m a.s.l..
354

355   *4.3 Thessaloniki*

356   Thessaloniki's multiwavelength Polarization Raman lidar system (THELISYS) belongs to the
357   Laboratory of Atmospheric Physics that is located at the Physics Department of the Aristotle
358   University of Thessaloniki (lat = 40.63° N, lon = 22.96° E, a.s.l. = 50m). Thessaloniki is a member
359   station of the EARLINET since 2000, providing almost continuous measurements, according to the
360   network schedule (every Monday morning, ideally close to 12:00 UTC, and every Monday and
361   Thursday evening) and during extreme events (e.g., Saharan dust outbreaks, smoke transport from
362   biomass burning, volcanic eruptions) and satellite overpasses. THELISYS has been validated within
363   EARLINET at hardware level by two intercomparison campaigns (Matthias et al., 2004), in order to
364   fulfill the standardized criteria. The system is based on the first (1064 nm), second (532 nm), and
365   third harmonic (355 nm) frequency of a compact, pulsed Nd:YAG laser emitted with a 10 Hz
366   repetition rate. THELISYS setup includes three elastic backscatter channels at 355, 532 and 1064nm,
367   two nitrogen Raman channels at 387 nm and 607nm, and two polarization sensitive channels at 532
368   nm. The acquisition system is based on a LICEL Transient Digitizer working in both the analogue
369   and photon counting (250 MHz) mode. The vertical resolution of the elastic raw signal at 355 nm is

370 equal to 3.75 m and is recorded in both analog and photon counting mode. The full overlap height is
371 almost 800m a.s.l. A detailed description of THELISYS can be found in Siomos et al. (2018) and
372 Voudouri et al. (2020).
373
374 *4.4. Aerosols' load variability in the vicinity of the PANACEA sites*

375   The variability of the atmospheric aerosol load in the vicinity of the three PANACEA stations
376 (Fig. 1-i) is discussed in this section. The aim of this introductory analysis is to investigate the
377 horizontal homogeneity of the aerosol optical depth (AOD) in the respective broader areas, playing a
378 key role in the comparison of ground-based and spaceborne profiles, which are not spatially
379 coincident as it will be shown in Section 5. For the purposes of this analysis, we have processed the
380 mid-visible (550 nm) columnar AOD retrievals, over the period 2008-2017, acquired by the MODIS
381 sensor, mounted on the Aqua polar orbiting satellite. More specifically, we have analyzed the Level
382 2 (L2; swaths; 5-min segments) MODIS-Aqua AODs, obtained by the latest version (Collection 6.1)
383 of the operational retrieval algorithms (Remer et al., 2008; Levy et al., 2013; Sayer et al., 2013). The
384 aforementioned data are accessible via the Level 1 and Atmosphere Archive and Distribution System
385 (LAADS) Distributed Active Archive Center (DAAC) (https://ladsweb.modaps.eosdis.nasa.gov/, last
386 access: 23 January 2023).

387   For each station, we have calculated the arithmetic mean of AODs within progressively larger
388 circular areas, with radii spanning from 10 to 100 km and with an incremental step of 10 km (Fig. 1-
389 ii). Figure 1-iii illustrates the resulting AODs for each station (x labels) and at each radius (colored
390 bars). In order to ensure the reliability of the obtained results, only the best (QA=3) MODIS-Aqua
391 AOD L2 retrievals are considered whereas the spatial averages (computed individually for each
392 circle) are calculated only when the satellite observations are simultaneously available at all circles.
393 In the urban areas of Athens (ATH) and Thessaloniki (THE), the contribution of anthropogenic
394 aerosols on the columnar load fades for increasing radii. On the contrary, at Antikythera (ANT), the
395 spatial AOD means remain almost constant revealing a horizontal homogeneity of the aerosol load in
396 the broader area. An alternative way to compare the differences in the AOD spatial representativeness
397 between the urban (ATH, THE) and the remote (ANT) sites has been performed. Fig. 1-iv illustrates
398 the normalized values for each radius with respect to the AOD levels of the inner circle (i.e., up to 10
399 km distance from the station). In both urban sites the values are lower than one (dashed line),
400 decreasing steadily in THE and smoothly in ATH after an abrupt reduction from 10 to 20 km. In
401 ANT, the blue curve resides almost on top of the dashed line throughout the circles radii (i.e., range
402 of distances) indicating the absence of significant horizontal variation of the aerosol load suspended
403 in the surrounding area.

409 A key aspect which has not been adequately addressed in Fig. 1-iii is the temporal variability
410 of aerosol loads since the spatiotemporally averaged AODs "hide" such information. A useful
411 measure for this purpose is the coefficient of variation (CV), defined as the ratio of the standard
412 deviation and the arithmetic mean of AOD (Anderson et al., 2003; Shinozuka and Redemann, 2011),
413 both calculated in temporal terms. Figure 1-v displays the CV values (expressed in percentage)
414 computed for each circle at each station. The highest levels (up to 90%) are recorded in Antikythera
415 whereas lower values (up to 70%) are recorded in THE and the lowest ones are found in ATH (up to
416 60%). This discrepancy is mainly attributed to the higher frequency of dust outbreaks affecting the
417 southern parts of Greece in contrast to the central and northern sectors of the country (Gkikas et al.,
418 2013; 2016). It is noted that all the PANACEA sites are also under the impact of advected loads
419 composed by anthropogenic/biomass particles originating at distant areas. Nevertheless, their
420 frequency of occurrence and their concentration is rarer and weaker, respectively, than those of the
421 advected Saharan dust. Between the remote (ANT) and urban (ATH, THE) sites there is clear
422 difference of the CV dependence with respect to the circle radius. In ANT, the CVs increase steadily
423 from the inner to the outer circle while an opposite tendency is found in THE and ATH. The increasing
424 trend in ANT is mainly regulated by the range of the Saharan plumes transported towards
425 southwestern Greece. On the contrary, the declining trend revealed in the two main Greek cities
426 indicates that the temporal variability of the local sources (i.e., two first circles) is more pronounced.
427 For completeness, we have also computed the spatial autocorrelation (Anderson et al., 2003;
428 Shinozuka and Redemann, 2011) among the averaged AODs of each circle area. The correlation
429 matrices for each station are presented in Fig. S1. Among the three PANACEA sites, the R values in
430 Athens (Fig. S1-i) drop rapidly, with respect to the first circle (10 km radius), highlighting the strong
431 spatial contrast of AODs between the city and the surrounding areas. For the outer domains, this
432 transition becomes significantly smoother and the R values are higher than 0.90 in most of the
433 combinations indicating a spatial coherence. In Thessaloniki (Fig. S1-iii), the pattern of the R values
434 onto the correlation matrix is similar with those of Athens but the high R values (> 0.89) indicate a
435 better spatial AOD homogeneity according to Anderson et al. (2003). Finally, under the absence of
436 local sources in Antikythera and strong AOD spatial homogeneity in the vicinity, the computed R
437 value between the inner (10 km radius) and the outer (100 km radius) circle is higher than 0.94 and
438 increases at shorter distances.

439

440 **5. Collocation between Aeolus and ground-based lidars**

441 The assessment of Aeolus SCA backscatter profiles has been performed against the
442 corresponding measurements acquired at the three EARLINET/PANACEA lidar stations. In Figure
443 2, three examples of the collocation between ground-based and spaceborne retrievals are illustrated

in order to describe our approach as well as to clarify points needed in the discussion of the evaluation results (Section 6). At each station, we identify the observations (BRCs), considering their coordinates at the beginning of the ALADIN scan, falling within a circle of 120 km radius (black dashed circle) centered at the station coordinates (black dot). Following this approach there is a possibility of including BRCs where more than half of their length to fall outside of the defined circle. This might affect the evaluation outcomes because we are not considering the BRC center in the collocation. Nevertheless, we are expecting a negligible impact on the statistical analysis since the 77% of the BRCs would have been selected using alternatively the coordinates at their center. Based on the defined spatial criterion the number of BRCs residing within the 120 km circle should be at least one and cannot be more than three. We denote each one of them, along the ALADIN measurement track (white stripe), with different colors (red, blue and magenta) in Fig. 2. The green arrow shows the flight direction of the satellite for the dusk (ascending) or dawn (descending) orbits. For the ground-based observations, the aerosol backscatter profiles are derived considering a time window of ± 1 hour around the satellite overpass. Nevertheless, this temporal collocation criterion has been relaxed or shifted in few cases to improve the quality of the ground-based retrievals (i.e., by increasing the signal-to-noise ratio) as well as to increase the matched pairs with Aeolus SCA profiles. Both compromises are applied since the weather conditions favoring the development of persistent clouds may eliminate the number of simultaneous cases. It is noted, however, when the temporal window is shifted or relaxed we are taking into account the homogeneity of the atmospheric scene (probed by the ground lidar). For the Antikythera station we did not deviate from the pre-defined temporal criterion apart from one case study. In Thessaloniki and Athens, the time departure between Aeolus and ground-based profiles can vary from 1.5 to 2.5 hours. Overall, 43 cases are analyzed out of which 15 have been identified over Antikythera, 12 in Athens and the remaining 16 in Thessaloniki.

The ground-based profiles are derived under cloud free conditions in contrast to Aeolus SCA backscatter profiles providing aerosol and/or cloud backscatter. Therefore, a cloud screening of the SCA data using auxiliary cloud information was applied. In the framework of the present study, the exclusion of cloud contaminated SCA profiles relies on the joint processing of the cloud mask product (CLM; https://www.eumetsat.int/media/38993; CLOUD MASK PRODUCT GENERATION) derived from radiances acquired by the SEVIRI (Spinning Enhanced Visible and Infrared Imager) instrument mounted on the Meteosat Second Generation (MSG) geostationary satellite (Schmetz et al., 2002). It should be noted, however, that the CLM product serves as an indication of clouds presence, without providing information about their macrophysical properties (i.e., cloud coverage), their phase (i.e., ice, water, mixed) or their categories (i.e., low, middle, high). According to the product user guide (https://www-cdn.eumetsat.int/files/2020-04/pdf_clm_pg.pdf; Section 3.4),

490 artificial straight lines can be found because the ECMWF temperature/humidity fields are not
491 interpolated in time and space. Moreover, due to the limited number of levels of ECMWF temperature
492 profiles, required for the atmospheric correction, the cloud detection in the lower troposphere is
493 impacted. Finally, broken clouds with limited spatial extension as well as thin cirrus are likely
494 misdetected by MSG. In the illustration examples of Figure 2, the grey shaded areas represent the
495 CLM spatial coverage at each PANACEA site. Based on the filtering procedures, the Aeolus SCA
496 backscatter retrievals, throughout the probed atmosphere by ALADIN, are removed from the analysis
497 when the grey shaded areas overlap with a BRC.

498
499 **6. Results**

500 *6.1 Assessment of Aeolus SCA backscatter under different aerosol scenarios*

501   In the first part of the analysis we assess the quality of the Aeolus SCA backscatter under
502 various aerosol regimes aiming to: (i) investigate the capabilities of the ALADIN spaceborne lidar to
503 detect aerosol layers, (ii) investigate how the horizontal homogeneity and vertical structure of the
504 aerosol layers can affect the level of agreement between spaceborne and ground-based retrievals and
505 (iii) demonstrate the synergistic use of various datasets for a better characterization of the prevailing
506 aerosol conditions. All of these aspects are necessary towards a comprehensive Cal/Val study to
507 facilitate the interpretation of our findings and to identify possible upgrades on SCA retrievals.
508 Overall, four cases over the Antikythera island (southwest Greece) are analyzed for the Aeolus SCA
509 aerosol backscatter retrievals (Baseline 2A11). The obtained results are depicted in Figure 3. The
510 identified cases have been selected because they are representing some of the most typical aerosol
511 conditions in the E. Mediterranean. Note that for each case we are selecting the nearest Aeolus BRC
512 to station coordinates that falls entirely within the circle area.

513   As it has been already mentioned, SCA retrievals are provided at coarse spatial (BRC level;
514 ~90 km) and vertical (minimum 250 m) resolution, while currently there is no scene classification
515 scheme. In order to overcome this inherent limitation, as much as possible, several ancillary data and
516 products are utilized in parallel with those of the MSG-SEVIRI CLM product. Based on the
517 FLEXPART v10.4 Lagrangian transport model (Stohl et al., 2005; Ignacio Pisso et al., 2019) we have
518 reproduced the 5-day air masses backtrajectories prior to their arrival at 7 altitudes above the ground
519 station. FLEXPART was driven with 3-hourly meteorological data from the National Centers for
520 Environmental Prediction (NCEP) Global Forecast System (GFS) analyses provided at 0.5° × 0.5°
521 resolution   and   for   41   model   sigma   pressure   levels
522 (https://nomads.ncep.noaa.gov/txt_descriptions/GFS_half_degree_doc.shtml). To depict the spatial
523 patterns of the mid-visible (550 nm) total and speciated AOD, we are relying on the MERRA-2

(Modern-Era Retrospective analysis for Research and Applications version 2; Buchard et al., 2017; Randles et al., 2017; Gelaro et al., 2017) and CAMS (Copernicus Atmosphere Monitoring Service; Inness et al., 2019) reanalysis datasets, both providing AODs of high quality (Gueymard and Yang, 2020; Errera et al., 2021). Finally, AERONET sun-direct measurements (Level 2.0, Version 3; Giles et al., 2019; Sinyuk et al., 2020) of spectral AODs and Ångström exponent as well as the Fine Mode Fraction (FMF at 500nm) derived from the spectral deconvolution algorithm (O'Neill et al., 2003) are also used for the characterization of the aerosol load and size over the station.

6.1.1 Dust advection on 10th of July 2019

The first case refers to the advection of dust aerosols from northwest Africa towards Antikythera with dust-laden air masses crossing southern Italy prior to their arrival from northwest directions (Figure S2). This route of air masses, driven by the prevailing atmospheric circulation (Gkikas et al., 2015), is typical during summer when Saharan aerosols are advected towards the eastern Mediterranean (Balis et al., 2006). MERRA-2 (Fig. S3-i) and CAMS (Fig. S3-ii) show a reduction of AODs (at 550nm) from west to east whereas the large contribution (>80%) of dust aerosols to the total aerosol load is evident in both reanalysis products (results not shown here). The moderate-to-high AOD values are confirmed by the ground-based sunphotometric measurements (Fig. S4) which are associated with low Ångström exponent (calculated between 440 nm and 870 nm) values (0.2 – 0.4) and FMF (Fig. S5) lower than 0.35 thus indicating the prevalence of coarse mineral particles (Dubovik et al., 2002). This is further supported from Polly^{XT} measurements (Fig. S6) revealing persistent dust layers associated with volume linear depolarization ratio (VLDR) values of 5-10% at 355 nm, stretched from altitudes close to the ground and up to almost 6 km.

This case is suitable for evaluating SCA backscatter retrievals since non-spherical mineral particles are probed by ALADIN, which does not detect the cross-polar component of the backscattered lidar signal. Therefore, a degradation of ALADIN's performance is expected (i.e., underestimation of the backscatter coefficient and overestimation of the lidar ratio) when aspherical particles (e.g., dust, volcanic ash, cirrus ice crystals) are probed. In Figure 3, the SCA backscatter coefficient step-like vertical profiles at the regular (brown) and mid-bin (black) vertical scales are compared against those acquired by the Polly^{XT} (pink) at 355 nm. The colored dashed lines (Aeolus) and the pink shaded area (Polly^{XT}) correspond to the statistical uncertainty margins of the spaceborne (see Section 2.3.1 in Flament et al., (2021)) and the ground-based (D'Amico et al., 2016) retrievals, respectively. Both refer to the photocounting noise following a Poisson distribution. At a first glance, it is evident that the geometrical structure of the dust layer, extending from 1 to 6 km, is generally well captured by ALADIN (except at altitude ranges from 1 to 2.5 km), but the backscatter magnitude

is constantly lower. A fairer comparison requires the conversion of the backscatter retrievals assuming that Polly^{XT} emits circularly polarized radiation (instead of linearly polarized) thus resembling ALADIN. Under the assumption of randomly oriented particles and negligible multiple scattering effects, this transformation is made based on theoretical formulas (Mishchenko and Hovenier, 1995; Roy and Roy, 2008), as it has been shown in Paschou et al. (2022). Following this approach, the Aeolus-like backscatter (i.e., circular co-polar component; blue curve in Fig. 3) is reproduced for the ground-based profiles at altitudes where UV depolarization measurements are available. Thanks to this conversion, the Aeolus-Polly^{XT} departures diminish and the Aeolus-like curve resides closer to those of SCA (brown) and SCA mid-bin (black) backscatter levels. The difference between pink and blue backscatter profiles, ranging from 13 to 33% in this specific case, reflects the underdetermination of the particle backscatter coefficient in case of depolarizing aerosols being probed, due to the missing cross-polar backscatter component.

6.1.2 Long-range transport of fine aerosols on 3rd July 2019

Under the prevalence of the Etesian winds (Tyrlis and Lelieveld, 2013), anthropogenic aerosols from megacities (Kanakidou et al., 2011) and biomass burning particles originating in the eastern Europe (van der Werf et al., 2017) are transported southwards. Based on the FLEXPART simulations (Fig. S7), the air masses carrying fine particles, gradually descend till their arrival over Antikythera from north-northeastern directions. During early morning hours, when ALADIN probes the atmosphere at a distance of ~90 km westwards of the ground station (dawn orbit; descending), moderate AODs (up to 0.15 at 340 nm), very high Ångström exponent values (>1.2) and FMFs varying from 0.6 to 0.7 are measured with the Cimel sunphotometer (Fig. S8 and Fig. S9). The aerosol load is confined below 2.5 km consisting of spherical particles as it is revealed from the Polly^{XT} volume linear depolarization ratio (VLDR) values, which do not exceed 5% at 355 nm (Fig. S10). In the vicinity of the PANGEA observatory, MERRA-2 (Fig. S11-i) and CAMS (Fig. S11-ii) AODs, mainly attributed to organic carbon, sulphate and sea-salt aerosols, do not exceed 0.2 and they are coherent in spatial terms (i.e., horizontal homogeneity). In this case, Polly^{XT} particle backscatter coefficient profiles coincide with the corresponding Aeolus-like profiles (pink and blue curves are almost overlaid in Fig. 3-ii) since depolarization values are negligible. Under these conditions, ALADIN is capable of reproducing satisfactorily the layer's structure whereas slightly overestimates its intensity with respect to the ground-truth retrievals.

6.1.3 Long range transport of fine aerosols on 8th July 2020

Deleted: underestimated

Deleted: 1

Deleted: negative biases

On 8th July 2020, the broader area of the Antikythera island was under the impact of moderate-to-high aerosol loads, mainly consisting of organic and sulphate particles, in the western and southern sector of the station, based on CAMS simulated AODs (up to 0.5) (Fig. S12-ii). AERONET measurements yield UV AODs up to 0.5 and Ångström exponent higher than 1.5 during early afternoon (Fig. S13) whereas the FMF is higher than 0.75 throughout the day (Fig. S14). MERRA-2 AOD patterns (Fig. S12-i) and speciation (strong contribution from marine and sulphate aerosols to the total aerosol load) are different from those of CAMS, without being very consistent with respect to the ground-based sunphotometer observations (Fig. S13, Fig. S14). Air masses originating in northern Balkans and the Black Sea, after crossing metropolitan areas (i.e., Istanbul, Athens), are advected over ANT at altitudes up to 4 km above surface. A second cluster aloft (>5 km) indicates the convergence of air masses from northwest (Fig. S15). In vertical terms, aerosol layers with local backscatter maxima gradually reducing from 3.5 to 1.5 Mm^{-1} sr^{-1} are observed up to 4 km based on Polly^{XT} backscatter coefficient profiles (pink curve, Fig. 3-iii) whereas almost identical values are recorded for the Aeolus-like retrievals (blue curve, Fig. 3-iii) under low VLDR levels (Fig. S16). For this specific case, SCA performance reveals an altitude dependency according to the comparison versus Polly^{XT}. From top to bottom, the weak layer extending from 6 to 8 km, observed in the ground-based lidar profiles is partially evident in the SCA retrievals. SCA fails to reproduce the aerosol layer (in terms of structure and backscatter magnitude) seen from the ground-based lidar between 2 and 4 km. Below 2 km, the agreement between ALADIN and Polly^{XT} becomes better, particularly for SCA mid-bin, even though the narrow peak recorded at ~1.2 km by Polly^{XT} cannot be reproduced by ALADIN. This might be attributed either to the adjusted RBS at the lowermost bin (1 km thickness) or to the lower accuracy of SCA retrievals near the ground due to the attenuation from the overlying layers (Flament et al., 2021).

6.1.4 Stratification of spherical and non-spherical particles on 5th August 2020

In the last case, that took place on 5th August 2020, we are investigating the ability of SCA to reproduce adequately the vertical structure of an aerosol layer detected up to 4 km based on Polly^{XT} (Fig. 3-iv; pink curve). The "peculiarity" of this study case, as it is revealed by the Polly^{XT} time-height plots of VLDR (Fig. S17), is that spherical fine particles dominate below 2.5 km whereas the presence of non-spherical coarse aerosols above this layer is evident. This stratification results from the convergence of air masses either originating in central Europe or suspending most of their travel above northwest Africa (Fig. S18). According to MERRA-2 (Fig. S19-i) and CAMS (Fig. S19-ii) reanalysis datasets, AODs fade from west to east while both numerical products indicate the coexistence of carbonaceous, sulphate and mineral particles over the area where ALADIN samples

the atmosphere (~100 km westwards of Antikythera). During the Aeolus overpass (~04:40 UTC), sunphotometer columnar observations are not available (Fig. S20, Fig. S21). However, one hour later, UV AODs up to 0.4 are recorded and remain relatively constant during sunlight hours. At the same time, intermediate Ångström (0.7 – 1) and FMF (~0.5) values, exhibiting weak temporal variation, indicate a mixing state of fine and coarse aerosols.

The SCA backscatter retrievals at the regular (i.e., SCA; brown curve; Fig. 3-iv) and the mid-bin (i.e., SCA mid-bin; black curve; Fig. 3-iv) vertical scales suffer from noise and retrieval gaps. As a result, Aeolus possibly (acknowledging the weak signals and the underestimated errors) detects incorrectly an aerosol layer between 5.5 and 8 km under the assumption that clear-sky conditions are appropriately represented in the MSG-SEVIRI imagery and remain constant within the time interval (~6 minutes) of MSG and Aeolus observations. At lower altitudes (2.5 – 4 km), due to the suspension of depolarizing mineral particles, a departure is marked between the pink (linear-derived) and blue (Aeolus-like) Polly^{XT} profiles. Both SCA and SCA mid-bin fail to reproduce the backscatter levels of this aerosol layer captured from the ground. In the lowest troposphere (< 2km), SCA overestimates significantly the backscatter coefficient but reproduces satisfactorily the aerosol layer structure at the mid-bin vertical scale (i.e., SCA mid-bin; black curve; Fig. 3-iv), in contrast to the regular scale (i.e., SCA; brown curve; Fig. 3-iv).

A general remark that should be made, is that for the cases analyzed, between the ground-based and spaceborne profiles there is an inconsistency in the vertical representativeness within the lowermost Aeolus bin. Under the absence of the near-field receivers (not considered in our study) Polly^{XT} profiles are reported above ~800 m where the overlap between the laser beam and the receiver telescope field of view is expected to be full. However, the base altitude of the near-surface Aeolus bin is at ~200 m. This can interpret, at some degree, the large positive ALADIN-Polly^{XT} departures at altitudes below 1 km, which are possibly further strengthened by an inappropriate RBS (i.e., low SNR) in the SCA retrievals.

6.2 Overall assessment and dependencies

In the second part of the analysis, an overall assessment of the Aeolus SCA retrievals is performed by processing all the identified cases (43 in total; see Section 5). Due to the very limited availability of ground-based extinction profiles, only the Aeolus SCA backscatter observations are evaluated. It must be clarified that the evaluation of the Aeolus satellite (SAT) backscatter coefficient is conducted without any conversion (i.e., from total linear to circular co-polar) of the ground-based lidar (GRD) profiles. This has been decided since many of the SAT-GRD collocated samples are derived from the Thessaloniki station. Due to technical issues (related to the polarization purity of the

Deleted: Aeolus

Deleted: Aeolus

Deleted: Aeolus

Deleted: L2A

Deleted: L2A

emitted laser beam and the performance of the telescope lenses) no calibrated depolarizing measurements, necessary to derive the Aeolus-like products (Paschou et al., 2022), are available for the study period. Nevertheless, we are not expecting that this consideration, acknowledging that it is imperfect, will affect substantially the robustness of our findings since in most of the study cases the contribution of depolarizing particles is quite low based on the ancillary datasets/products. It is also clarified that the Aeolus QA flags are not taken into account in the current study, since their validity is not yet reliable (Reitebuch et al., 2020) as it has been demonstrated in Abril-Gago et al. (2022). The discussion in the current section is divided in two parts. First, the vertically resolved evaluation metrics are presented separately for the two Aeolus vertical scales, both for the unfiltered and the filtered (cloud-free) profiles (Section 6.2.1). The same analysis format (i.e., SCA vs SCA mid-bin, unfiltered vs filtered) is kept in the second sub-section (Section 6.2.2) where the evaluation results are presented as a function of various dependencies.

6.2.1 Vertically resolved evaluation metrics

In Figure 4, the vertically resolved bias (SAT-GRD; upper panel) and root mean square error (RMSE; bottom panel) metrics are depicted for the unfiltered (cloud and aerosol backscatter) Aeolus SCA backscatter retrievals, reported at the regular (left column) and the mid-bin (right column) vertical scales. Bias and RMSE metrics (Wilks, 2019) are used in a complementary way in order to avoid any misleading interpretation of the former score attributed to counterbalancing negative and positive SAT-GRD deviations. For the calculation of the evaluation scores, the GRD profiles have been rescaled to match Aeolus vertical product resolution. To realize, we are calculating the averaged values of the ground-based retrievals residing within the altitude margins of each Aeolus BRC. Note that in the SAT-GRD pairs, all BRCs from all cases are included (right y-axis in Figure 4), satisfying the defined collocation criteria (see Section 5), and they are treated individually. It is reminded that Aeolus L2A data are provided vertically at a constant number of range bins (i.e., 24 for SCA and 23 for SCA mid-bin) but their base altitude and their thickness vary along the orbit and from orbit-to-orbit and they are defined dynamically (depending on the optimum SNR). Therefore, since the GRD and SAT profiles are not interpolated in a common predefined grid, we are using as reference the reverse index (with respect to those considered in the SCA retrieval algorithm in which 1 corresponds to the top-most bin) of Aeolus SCA (from 1 to 24; left y-axis in Figs 4 i-a and ii-a) and SCA mid-bin (from 1 to 23; left y-axis in Figs 4 i-b and ii-b) vertical scales.

According to our results for the unfiltered SCA backscatter profiles (Fig. 4), positive biases (up to 3.5 Mm^{-1} sr^{-1}; red bars) are evident, at both vertical scales, at the first three bins (below 2 km). For altitude ranges spanning from 2 to 8 km (bins 4 – 12), mainly positive SAT-GRD biases (up to

724 ~1.5 Mm^{-1} sr^{-1}) are recorded for SCA mid-bin whereas for SCA reach up to ~1 Mm^{-1} sr^{-1} in absolute

725 terms. Similar tendencies are evident at the highest altitudes (> 8 km) but the magnitude of the SAT-

726 GRD offsets becomes lower (< 0.5 Mm^{-1} sr^{-1}). Between the two Aeolus vertical scales, SCA mid-bin

727 RMSE metrics are better than those of SCA up to ~8 km (bin 12) and similar aloft (bottom panel in

728 Fig. 4). Nevertheless, the most important finding is that SCA is not capable to reproduce satisfactorily

729 the backscatter profiles as it is revealed by the RMSE levels, which are maximized near the ground

730 (~ 8 Mm^{-1} sr^{-1}), are considerably high (up to 6 Mm^{-1} sr^{-1}) in the free troposphere and are minimized

731 (< 1 Mm^{-1} sr^{-1}) at the uppermost bins. Our findings are highly consistent with those presented in

732 Abril-Gago et al. (2022), who performed a validation of Aeolus SCA particle backscatter coefficient

733 against reference measurements obtained at three ACTRIS/EARLINET sites in the Iberian Peninsula.

734 Several factors contribute to the obtained height-dependent SAT-GRD discrepancies. Near the

735 ground, the observed maximum overestimations are mainly attributed to the: (i) contamination of the

736 ALADIN lidar signal by surface reflectance, (ii) increased noise in the lowermost bins (caused by the

737 non-linear approach retrieving the backscatter coefficient) as it has been pointed out also in the

738 atmospheric simulations cases I and II in Ehlers et al. (2022) and (iii) limited vertical

739 representativeness of the GRD profiles below 1 km. On the contrary, in the free troposphere, the cloud

740 contamination on spaceborne retrievals plays a dominant role on the occurrence of ALADIN

741 backscatter overestimations with respect to the cloud-free ground-based retrievals. From a statistical

742 point of view, it must also be mentioned that the robustness of the bias and RMSE metrics decreases

743 for increasing altitudes due to the reduction of the number of the SAT-GRD matchups (right y-axis

744 in Fig. 4) participating in the calculations.

745   The assessment analysis has been repeated after removing SCA profiles when clouds are

746 detected by MSG-SEVIRI (grey shaded areas in Fig. 1) within a BRC (colored rectangles in Fig. 1).

747 By contrasting Figures 4 and 5 (evaluation metrics for the filtered profiles), an expected improvement

748 of the level of agreement between SAT and GRD is visible. This translates into a drastic reduction of

749 bias and RMSE levels at altitude ranges up to 5-6 km (~bin 10). Between bins 2 and 5 slight

750 underestimations (blue bars) and overestimations (red bars) are found for SCA (Fig. 5 i-a). On the

751 contrary, for the SCA mid-bin (Fig. 5 i-b) low positive SAT-GRD offsets are recorded due to the

752 omitted negative backscatter values, as it will be shown in the next section. Above bin 5, SAT-GRD

753 deviations are low in absolute terms, oscillating around zero, for SCA, whereas only positive SAT-

754 GRD biases are recorded for SCA mid-bin, which are maximized (~ 0.7 Mm^{-1} sr^{-1}) at the highest bins

755 and are associated with limited SAT-GRD matchups (right x-axis in Fig. 5 i-b). The obtained

756 improvements on bias scores become more confident since they are associated with similar strong

757 reductive tendencies on RMSE levels. More specifically, the RMSE spikes of extremely high values

Deleted: performs

Deleted: , as it is shown by the RMSE profiles

Deleted: Aeolus

Deleted: L2A

Deleted: the

Deleted: Aeolus

recorded in the unfiltered profiles either disappear or weaken in the case of the Aeolus filtered SCA (Fig. 5 ii-a) and SCA mid-bin (Fig. 5 ii-b) backscatter profiles. However, even though the RMSE values at the lowermost bins (close to the ground) are decreased when cloud contaminated Aeolus profiles are eliminated, still the corresponding levels for the filtered profiles are considerably high attributed to the lower SNR and the possible impact of surface returns.

6.2.2 Scatterplots

An alternative approach to assess the performance of Aeolus SCA backscatter is attempted here by reproducing two dimensional histograms for the entire SAT-GRD collocated sample as well as scatterplots resolved based on various dependencies. More specifically, the dependencies under investigation are those of the: (i) station locations, (ii) BRCs and (iii) orbits (dawn vs dusk). The evaluation metrics have been calculated for all possible combinations of vertical scales (SCA vs SCA mid-bin) and SCA profiles (unfiltered vs filtered).

Figure 6 depicts the two-dimensional histograms between GRD (x-axis) and SAT (y-axis) backscatter coefficient for the raw (upper panel) and filtered (bottom panel) SCA profiles reported at the SCA (left column) and SCA mid-bin (right column) vertical scales. Note that we have removed SAT-GRD pairs in which SCA backscatter exceeds 20 Mm^{-1} sr^{-1} in order to avoid the "contamination" of extreme outliers in the calculated metrics, possibly attributed to the presence of clouds (Proestakis et al., 2019).

Between the SCA and SCA mid-bin unfiltered retrievals, it is found that the correlation coefficients (0.36 and 0.39, respectively) and RMSEs (2.00 and 1.88, respectively) are similar whereas there is an evident difference on the biases (0.45 Mm^{-1} sr^{-1} and 0.69 Mm^{-1} sr^{-1}, respectively). Nevertheless, it is noted that less SAT-GRD pairs are recorded for SCA mid-bin due to the inherent flagging of negative values. After removing cloud-contaminated SCA profiles, the amount of the SAT-GRD matchups is reduced by about 55% and 59% for SCA (from 537 to 239) and SCA mid-bin (from 356 to 147), respectively. Nevertheless, thanks to this filtering procedure, the initially observed overestimations for SCA and SCA mid-bin are reduced by ~25% and ~43%, respectively, whereas the RMSE values drop down to 1.65 (SCA) and 1.00 (SCA mid-bin). The better agreement between SAT and GRD, for the filtered SCA profiles, is further justified by the increase of the R values (from 0.39 to 0.48) for the SCA mid-bin whereas for SCA there is no positive or negative tendency (R=0.36). The spread of the points in the two dimensional space reveals many similarities with the corresponding scatterplots presented in Abril-Gago et al. (2022) for the Iberian ACTRIS/EARLINET stations.

807 A common feature in all scatterplots, shown in Figure 6, is that most of the positive outliers

808 are found at the lowermost bins (see Figs. 4 and 5). SAT beta can reach up to 20 $\text{Mm}^{-1}\ \text{sr}^{-1}$ in contrast

809 to the corresponding GRD levels, which are mainly lower than 2 $\text{Mm}^{-1}\ \text{sr}^{-1}$. For SCA (Figs. 6 i-a, 6

810 ii-a), the majority of the negative SAT-GRD pairs are recorded at the highest bins in which, however,

811 both spaceborne and ground-based backscatter coefficients are noisy. Another cluster of SAT-GRD

812 pairs is those where slight negative SCA backscatter values are grouped together with low positive

813 backscatter values retrieved from ground. At the mid-bin vertical scale, for the unfiltered SCA profiles

814 (Fig. 6 i-b), the negative SAT backscatter values are masked out resulting in better evaluation metrics

815 (except the increase of bias due to the removal of the negative SCA backscatter) with respect to the

816 regular vertical scale. Among the four scatterplots, the best agreement between SCA and ground-

817 based retrievals is revealed for the SCA mid-bin filtered profiles (Fig. 6 ii-b) attributed to the

818 coincident elimination of the negative and the extreme positive SCA backscatter coefficient.

819 Figure 7 depicts the overall scatterplot between ground-based and spaceborne retrievals as a

820 function of the three PANACEA sites (colored categories). The associated evaluation scores are

821 summarized in Table 1 and 2 for the unfiltered and filtered SCA profiles, respectively. The majority

822 of the extreme positive outliers of unfiltered SCA retrievals (Fig. 7 i-a) are recorded in Thessaloniki

823 and Athens. According to our results, for SCA, significant biases (0.73 $\text{Mm}^{-1}\ \text{sr}^{-1}$ for ATH and 0.83

824 $\text{Mm}^{-1}\ \text{sr}^{-1}$ for THE) and high RMSE values (2.26 $\text{Mm}^{-1}\ \text{sr}^{-1}$ for ATH and 2.60 $\text{Mm}^{-1}\ \text{sr}^{-1}$ for THE) are

825 found. At Antikythera island (ANT), the biases are quite low and equal to 0.06 $\text{Mm}^{-1}\ \text{sr}^{-1}$ and 13.6%

826 in absolute and relative terms, respectively (Table 1). In all stations, for the unfiltered SCA mid-bin

827 retrievals, the absolute SAT-GRD departures become larger whereas the RMSE decreases in

828 ANT/THE and increases in ATH. Regarding the temporal covariation between SAT and GRD

829 retrievals, a noticeable improvement is evident in ANT (i.e., R increases from 0.49 to 0.57). For the

830 quality-assured SCA profiles (Table 2), all evaluation metrics converge towards the ideal scores for

831 SCA mid-bin whereas mainly positive tendencies (i.e., better agreement) are evident for SCA.

832 Overall, among the three stations the best performance of the SCA retrievals is recorded at the

833 Antikythera island.

834 Between dawn (descending) and dusk (ascending) orbits, better bias and RMSE scores are

835 computed when Aeolus is flying during early morning hours while better R values are found during

836 early afternoon satellite overpasses. However, our orbit-wise results are not robust since the number

837 of Aeolus overpasses is not evenly distributed (about 85% of the SAT-GRD matchups are acquired

838 during dawn orbits). Among the three BRCs (red, blue or magenta), which can satisfy the defined

839 SAT-GRD spatial criterion (see Section 5) the best metrics are found for the red BRC residing most

840 of the cases closer to the station site.

849

7. Discussion on Cal/Val aspects and recommendations

851

Throughout this assessment analysis, several critical points have been identified and highlighted that should be addressed adequately towards a comprehensive Cal/Val study of the Aeolus SCA products. These aspects can: (i) serve as guidelines for future relevant studies, (ii) improve our understanding about the advantages/limitations of Aeolus data in terms of their usefulness and applicability in aerosol-related studies and (iii) suggest possible upgrades regarding ALADIN's observational capabilities, the considerations of the applied retrieval algorithms and the content of information in Aeolus SCA data.

A fair comparison of Aeolus SCA backscatter versus linear-derived retrievals acquired from ground-based lidars, when depolarizing particles are recorded, requires the conversion of the latter ones to circular co-polar (Aeolus-like) following Paschou et al. (2022). Nevertheless, it should be acknowledged that the theoretical assumptions can be invalid either due to the orientation of the suspended particles (e.g., mineral dust; Ulanowski et al., 2007; Daskalopoulou et al., 2021; Mallios et al., 2021) or due to multiple scattering effects within optically thick aerosol layers (Wandinger et al., 2010). The lack of aerosols/clouds discrimination in Aeolus SCA data forces the synergistic implementation of ancillary data in order to remove cloud contaminated Aeolus profiles from the collocated sample with the cloud-free ground-based profiles. Nevertheless, it should be noted that the cloud removal itself is not perfect. In our case, we are relying on MSG-SEVIRI cloud observations, which are available at high temporal frequency (every 15 min) thus allowing a very good temporal collocation with Aeolus. The indirect cloud-mask filtering applied to our analysis, leads to a substantial improvement of the level of agreement between spaceborne and ground-based retrievals. Despite its success, our proposed approach provides a sufficient and acceptable solution, but undoubtedly cannot be superior to the utility of a descriptive classification scheme on Aeolus retrieval algorithms similarly done in CALIOP-CALIPSO (Liu et al., 2019; Zeng et al., 2019).

Aeolus retrievals are available at coarse along-track resolution (~90 km). This imposes limitations on their evaluation against point measurements, which are further exacerbated at sites where the heterogeneity of aerosol loads in the surrounding area of the station is pronounced, taking into account that the spatial collocation between spaceborne and ground-based retrievals is not exact. Numerical outputs from reanalysis datasets (e.g., MERRA-2, CAMS) can be utilized as an indicator of aerosols' burden horizontal variation, taking advantage of their complete spatial coverage, their availability at high temporal frequency and their reliability in terms of total AOD (Innes et al., 2019; Gueymard and Yang, 2020). Nevertheless, such data are better to be utilized in a qualitative rather

---

than a quantitative way, particularly in terms of aerosol species, since they cannot be superior of actual aerosol observations. Over areas with a complex terrain, vertical inconsistencies between ground-based and satellite profiles (reported above ground where its height is defined with respect to the WGS 84 ellipsoid), not physically explained, can be recorded. For the derivation of the evaluation scores, it is required a rescaling of the ground-based profiles, acquired at finer vertical resolution, in order to match the dynamically defined Aeolus' range bin settings. Nevertheless, due to this transformation, the shape of the raw ground-based profile can be distorted and the magnitude of the retrieved optical properties can be modified substantially thus affecting the evaluation metrics. This artifact is evident in cases where the vertical structure of the aerosol layers is highly variable thus hindering Aeolus capability to reproduce accurately their geometrical features. Finally, the consideration of backward trajectories can assist the characterization of the probed atmospheric scene by Aeolus. Potentially, they can be also used as an additional criterion for the optimum selection of Aeolus BRC for the collocation with the ground-based measurements. However, possible limitations may arise due to temporal deviations among FLEXPART run, the Aeolus overpass and ground-based retrievals, which might be critical taking into account the strong spatiotemporal variability of aerosol loads across various scales.

8. Conclusions

The limited availability of vertically resolved aerosol products from space constitutes a major deficiency of the Global Observing System (GOS). The launch of the Aeolus ESA satellite was a major step towards this direction whereas the forthcoming EarthCARE satellite mission (Illingworth et al., 2015) will accelerate further these efforts. ALADIN, the single payload of the Aeolus satellite, constitutes the first UV HSRL Doppler lidar ever placed in space and it is optimized to acquire HLOS wind profiles towards advancing numerical weather prediction (Rennie et al., 2021). ALADIN also retrieves independently the extinction and backscatter coefficients of aerosols and clouds (grouped as particulates according to Aeolus' nomenclature) via the implementation of various retrieval algorithms (SCA, MLE, AEL-PRO).

The current work focuses on the assessment of the SCA backscatter coefficients versus ground-based retrievals acquired routinely by lidar systems operating in Athens, Thessaloniki, and Antikythera. The aforementioned stations contribute to the PANACEA Greek National Research Infrastructure (Greek ACTRIS component) and to the European Aerosol Research Lidar Network (EARLINET; Pappalardo et al., 2014). Overall, 43 cases are analyzed out of which 12 have been identified in the urban site of Athens, 16 in Thessaloniki and 15 in the remote site of the Antikythera island.

In the first part of the analysis, focus was given on the assessment of Aeolus SCA particle backscatter coefficient, under specific aerosol scenarios, versus the corresponding measurements obtained at the Antikythera island (southwest Greece). The misdetection of the cross polarized lidar return signals can interpret the lower Aeolus SCA backscatter values (ranging from 13% to 33%) with respect to ground-based retrievals when depolarizing mineral particles are probed (case of 10th July 2019). For the case of 3rd July 2019, when aerosol loads of moderate intensity, consisting mainly of spherical particles, are confined below 4 km and they are homogeneous in the surrounding area of the station, Aeolus' SCA backscatter product is capable in reproducing quite well the ground-based profile in terms of shape and magnitude. For the cases of 8th July 2020 and 5th August 2020, SCA performance in terms of depicting complex stratified aerosol layers (composed of particles of different origin), as these are observed from ground, degrades due to noise in the cross-talk corrected molecular and particulate signals.

Our statistical assessment analysis reveals that the removal of cloud contaminated spaceborne profiles, achieved via the synergy with MSG-SEVIRI cloud observations, results in a significant improvement of the product performance. Unfortunately, the poor evaluation metrics at the lowermost bins (attributed to either the surface reflectance or the increased noise levels for the Aeolus retrievals and to the overlap issues for the ground-based profiles) are still evident after the cloud filtering procedure. Between the two Aeolus vertical scales, the computed evaluation metrics do not provide strong evidence of which of them performs better. Among the three stations (ATH, ANT, THE) considered here, the best agreement was found in the remote site of Antikythera island in contrast to the urban sites of Athens and Thessaloniki. All key Cal/Val aspects, serving as guidelines and potential recommendations for future studies, have been discussed thoroughly.

In the current work, we emphasized only on the particle backscatter coefficient due to the limited number of ground-based extinction profiles. A wider assessment analysis is ongoing in the framework of the Aeolus L2A Cal/Val study performed within EARLINET. Finally, the best assessment of Aeolus L2A products is expected versus the purpose-built eVe lidar (Paschou et al., 2022). Thanks to its configuration, eVe can mimic Aeolus' observational geometry and test the validity of the theoretical formulas applied for the derivation of the Aeolus-like backscatter from the linearly polarized emission ground-based systems. The first correlative Aeolus-eVe measurements have been performed in the framework of the Joint Aeolus Tropical Atlantic Campaign (JATAC), that took place in Cape Verde in September 2021. Correlative measurements are also acquired during the ESA-ASKOS experimental campaign (Mindelo, Cabo Verde). The geographical location of Cabo Verde, situated on the "corridor" of the Saharan transatlantic transport (Gkikas et al., 2022), is ideal

for assessing Aeolus performance when non-spherical mineral particles from the nearby deserts are advected westwards.

Acknowledgments

Antonis Gkikas was supported by the Hellenic Foundation for Research and Innovation (H.F.R.I.) under the "2nd Call for H.F.R.I. Research Projects to support Post-Doctoral Researchers" (project acronym: ATLANTAS, project number: 544). Vassilis Amiridis acknowledges support from the European Research Council (grant no. 725698; D-TECT). NOA members acknowledge support from the Stavros Niarchos Foundation (SNF). We acknowledge support of this work by the project "PANhellenic infrastructure for Atmospheric Composition and climatE change" (MIS 5021516) which is implemented under the Action "Reinforcement of the Research and Innovation Infrastructure", funded by the Operational Programme "Competitiveness, Entrepreneurship and Innovation" (NSRF 2014-2020) and co-financed by Greece and the European Union (European Regional Development Fund). We thank the ACTRIS-2 and ACTRIS preparatory phase projects that have received funding from the European Union's Horizon 2020 Framework Program for Research and Innovation (grant agreement no. 654109) and from European Union's Horizon 2020 Coordination and Support Action (grant agreement no. 739530), respectively. This research was also supported by data and services obtained from the PANhellenic Geophysical Observatory of Antikythera (PANGEA) of the National Observatory of Athens (NOA). We acknowledge support by ESA, in the framework of the Aeolus+Innovation (Aeolus+I) call, under Contract No. 4000133130/20/I-BG//.

Data availability

Aeolus Baseline 11 L2A data were obtained from the ESA Aeolus Online Dissemination System available at https://aeolus-ds.eo.esa.int/oads/access/.

References

Abril-Gago, J., Guerrero-Rascado, J. L., Costa, M. J., Bravo-Aranda, J. A., Sicard, M., Bermejo-Pantaleón, D., Bortoli, D., Granados-Muñoz, M. J., Rodríguez-Gómez, A., Muñoz-Porcar, C., Comerón, A., Ortiz-Amezcua, P., Salgueiro, V., Jiménez-Martín, M. M., and Alados-Arboledas, L.: Statistical validation of Aeolus L2A particle backscatter coefficient retrievals over ACTRIS/EARLINET stations on the Iberian Peninsula, Atmos. Chem. Phys., 22, 1425–1451, https://doi.org/10.5194/acp-22-1425-2022, 2022.

Amiridis, V., Balis, D. S., Giannakaki, E., Stohl, A., Kazadzis, S., Koukouli, M. E., and Zanis, P.: Optical characteristics of biomass burning aerosols over Southeastern Europe determined from UV-Raman lidar measurements, Atmos. Chem. Phys., 9, 2431–2440, https://doi.org/10.5194/acp-9-2431-2009, 2009.

Amiridis, V., Giannakaki, E., Balis, D. S., Gerasopoulos, E., Pytharoulis, I., Zanis, P., Kazadzis, S., Melas, D., and Zerefos, C.: Smoke injection heights from agricultural burning in Eastern Europe as seen by CALIPSO, Atmos. Chem. Phys., 10, 11567–11576, https://doi.org/10.5194/acp-10-11567-2010, 2010.

Amiridis, V., Zerefos, C., Kazadzis, S., Gerasopoulos, E., Eleftheratos, K., Vrekoussis, M., Stohl, A., Mamouri, R.E., Kokkalis, P., Papayannis, A., et al.: Impact of the 2009 Attica wildfires on the air quality in urban Athens, Atmos. Environ., 46, 536–544, https://doi.org/10.1016/j.atmosenv.2011.07.056, 2012.

Amodeo, Aldo, D'Amico, Giuseppe, Giunta, Aldo, Papagiannopoulos, Nikolaos, Papayannis, Alex, Argyrouli, Athina, Mylonaki, Maria, Tsaknakis, Georgios, Kokkalis, Panos, Soupiona, Ourania, Tzanis, Chris. (2018). ATHLI16: the ATHens Lidar Intercomparison campaign. EPJ Web of Conferences. 176. 09008. 10.1051/epjconf/201817609008.

Anderson, T. L., Charlson, R. J., Winker, D. M., Ogren, J. A., and Holmén, K.: Mesoscale Variations of Tropospheric Aerosols, J. Atmos. Sci., 60, 119–136, https://doi.org/10.1175/1520-0469(2003)060<0119:MVOTA>2.0.CO;2, 2003.

Ansmann, A., Petzold, A., Kandler, K., Tegen, I., Wendisch, M., Müller, D., Weinzierl, B., Müller, T. and Heintzenberg, J.: Saharan Mineral Dust Experiments SAMUM–1 and SAMUM–2: what have we learned?, Tellus B: Chemical and Physical Meteorology, 63(4), 403–429, doi:10.1111/j.1600-0889.2011.00555.x, 2011.

Ansmann, A., Wandinger, U., Riebesell, M., Weitkamp, C., Michaelis, W.: Independent measurement of extinction and backscatter profiles in cirrus clouds by using a combined raman elastic-backscatter lidar, Applied Optics, 31, 7113-7131, doi: 10.1364/AO.31.007113, 1992.

Baars, H., et al. : An overview of the first decade of PollyNET: an emerging network of automated Raman-polarization lidars for continuous aerosol profiling, Atmos. Chem. Phys., 16, 5111–5137, https://doi.org/10.5194/acp-16-5111-2016, 2016.

Baars, H., Ansmann, A., Ohneiser, K., Haarig, M., Engelmann, R., Althausen, D., Hanssen, I., Gausa, M., Pietruczuk, A., Szkop, A., Stachlewska, I. S., Wang, D., Reichardt, J., Skupin, A., Mattis, I., Trickl, T., Vogelmann, H., Navas-Guzmán, F., Haefele, A., Acheson, K., Ruth, A. A., Tatarov, B., Müller, D., Hu, Q., Podvin, T., Goloub, P., Veselovskii, I., Pietras, C., Haeffelin, M., Fréville, P., Sicard, M., Comerón, A., Fernández García, A. J., Molero Menéndez, F., Córdoba-Jabonero, C., Guerrero-Rascado, J. L., Alados-Arboledas, L., Bortoli, D., Costa, M. J., Dionisi, D., Liberti, G. L., Wang, X., Sannino, A., Papagiannopoulos, N., Boselli, A., Mona, L., D'Amico, G., Romano, S., Perrone, M. R., Belegante, L., Nicolae, D., Grigorov, I., Gialitaki, A., Amiridis, V., Soupiona, O., Papayannis, A., Mamouri, R.-E., Nisantzi, A., Heese, B., Hofer, J., Schechner, Y. Y., Wandinger, U., and Pappalardo, G.: The unprecedented 2017–2018 stratospheric smoke event: decay phase and aerosol properties observed with the EARLINET, Atmos. Chem. Phys., 19, 15183–15198, https://doi.org/10.5194/acp-19-15183-2019, 2019.

Baars, H., Herzog, A., Heese, B., Ohneiser, K., Hanbuch, K., Hofer, J., Yin, Z., Engelmann, R., and Wandinger, U.: Validation of Aeolus wind products above the Atlantic Ocean, Atmos. Meas. Tech., 13, 6007–6024, https://doi.org/10.5194/amt-13-6007-2020, 2020.

Baars, H., Radenz, M., Floutsi, A. A., Engelmann, R., Althausen, D., Heese, B., Ansmann, A., Flament, T., Dabas, A., Trapon, D., Reitebuch, O., Bley, S., and Wandinger, U.: Californian wildfire smoke over Europe: A first example of the aerosol observing capabilities of Aeolus compared to ground-based lidar, Geophys. Res. Lett., 48, e2020GL092194, https://doi.org/10.1029/2020GL092194, 2021.

Balis, D., Amiridis, V., Nickovic, S., Papayannis, A., and Zerefos, C.: Optical properties of Saharan dust layers as detected by a Raman lidar at Thesaloniki, Greece, Geophys. Res. Lett., 31, L13104, https://doi.org/10.1029/2004GL019881, 2004

Balis, D., Amiridis, V., Kazadzis, S., Papayannis, A., Tsaknakis, G., Tzortzakis, S., Kalivitis, N., Vrekoussis, M., Kanakidou, M., Mihalopoulos, N., Chourdakis, G., Nickovic, S., Pérez, C., Baldasano, J., and Drakakis, M.: Optical characteristics of desert dust over the East Mediterranean

during summer: a case study, Ann. Geophys., 24, 807–821, https://doi.org/10.5194/angeo-24-807-2006, 2006.

Brioude, J., Arnold, D., Stohl, A., Cassiani, M., Morton, D., Seibert, P., Angevine, W., Evan, S., Dingwell, A., Fast, J.D., Easter, R.C., Pisso, I., Burkhart, J., Wotawa, G., 2013. The Lagrangian particle dispersion model FLEXPART-WRF version 3.1. Geosci. Model. Dev. 6, 1889e1904. http://dx.doi.org/10.5194/gmd-6-1889-2013.

Bohlmann, S., Baars, H., Radenz, M., Engelmann, R., and Macke, A.: Ship-borne aerosol profiling with lidar over the Atlantic Ocean: from pure marine conditions to complex dust–smoke mixtures, Atmos. Chem. Phys., 18, 9661–9679, https://doi.org/10.5194/acp-18-9661-2018, 2018.

Boucher, O., Randall, D., Artaxo, P., Bretherton, C., Feingold, G., Forster, P., Kerminen, V.-M., Kondo, Y., Liao, H., Lohmann, U., Rasch, P., Satheesh, S., Sherwood, S., Stevens, B., and Zhang, X.: Clouds and Aerosols, in: Climate Change 2013: The Physical Science Basis. Contribution of Working Group I to the Fifth Assessment Report of the Intergovernmental Panel on Climate Change, edited by Stocker, T., Qin, D., Plattner, G.-K., Tignor, M., Allen, S., Boschung, J., Nauels, A., Xia, Y., Bex, V., and Midgley, P., chap. 7, pp. 571–658, Cambridge University Press, Cambridge, United Kingdom and New York, NY, USA, https://doi.org/10.1017/CBO9781107415324.016, 2013.

Buchard, V., Randles, C. A., da Silva, A. M., Darmenov, A., Colarco, P. R., Govindaraju, R., Ferrare, R., Hair, J., Beyersdorf, A. J., Ziemba, L. D. and Yu, H.: The MERRA-2 aerosol reanalysis, 1980 onward. Part II: Evaluation and case studies, J. Climate, 30, 6851–6872, https://doi.org/10.1175/JCLI-D-16-0613.1, 2017.

Campbell, J. R., Hlavka, D. L., Welton, E. J., Flynn, C. J., Turner, D. D., Spinhirne, J. D., Scott, V. S., and Hwang, I. H.: Full-time eye-safe cloud and aerosol lidar observation at Atmospheric Radiation Measurement program sites: Instruments and data processing, J. Atmos. Oceanic Technol., 19, 431–442, 2002.

Charlson, R. J., Schwartz, S. E., Hales, J. M., Cess, R. D., Coakley, J. A., Hansen, J. E., and Hofmann, D. J.: Climate Forcing by Anthropogenic Aerosols, Science, 255, 423–430, https://doi.org/10.1126/science.255.5043.423, 1992.

Collis, R. and Russell, P.: Lidar measurement of particles and gases by elastic backscattering and differential absorption, chap. Lidar measurement of particles and gases by elastic backscattering and differential absorption, Springer, Berlin, Heidelberg, 71– 151, https://doi.org/10.1007/3-540-07743-X_18, 1976.

Dabas, A.: Generation of AUX_CAL: Detailed Processing Model and Input/Output Data Definition, software, ESA, available at: https://earth.esa.int/eogateway/documents/20142/ 1564626/Aeolus-Calibration-Processor-Documentation.zip (last access: 20 February 2022), 2017.

D'Amico, G., Amodeo, A., Mattis, I., Freudenthaler, V., and Pappalardo, G.: EARLINET Single Calculus Chain – technical – Part 1: Pre-processing of raw lidar data, Atmos. Meas. Tech., 9, 491– 507, https://doi.org/10.5194/amt-9-491-2016, 2016.

Daskalopoulou, V., Raptis, I. P., Tsekeri, A., Amiridis, V., Kazadzis, S., Ulanowski, Z., Metallinos, S., Tassis, K., and Martin, W.: Monitoring dust particle orientation with measurements of sunlight dichroic extinction, 15th International Conference on Meteorology, Climatology and Atmospheric Physics (COMECAP 2021), Ioannina, Greece, 26–29 September 2021, Zenodo [conference paper], https://doi.org/10.5281/zenodo.5075998, 2021.

Derrien, M. and Le Gleau, H.: MSG/SEVIRI cloud mask and type from SAFNWC, Int. J. Remote Sens., 26, 4707–4732, 2005.

Dubovik, O., Holben, B. N., Eck, T. F., Smirnov, A., Kaufman, Y. J., King, M. D., Tanré, D., and Slutsker, I.: Variability of Absorption and Optical Properties of Key Aerosol Types Observed in Worldwide Locations, J. Atmos. Sci., 59, 590–608, 2002.

ECMWF: ECMWF starts assimilating Aeolus wind data, https://www.ecmwf.int/en/about/media-centre/news/2020/ecmwf-starts-assimilating-aeolus-wind-data, last access: 12 June 2020, 2020.

Ehlers, F., Flament, T., Dabas, A., Trapon, D., Lacour, A., Baars, H., and Straume-Lindner, A. G.: Optimization of Aeolus' aerosol optical properties by maximum-likelihood estimation, Atmos. Meas. Tech., 15, 185–203, https://doi.org/10.5194/amt-15-185-2022, 2022.

1136 Engelmann, R., Kanitz, T., Baars, H., Heese, B., Althausen, D., Skupin, A., Wandinger, U.,
1137 Komppula, M., Stachlewska, I. S., Amiridis, V., Marinou, E., Mattis, I., Linné, H., and Ansmann, A.:
1138 The automated multiwavelength Raman polarization and water-vapor lidar Polly[XT]: the neXT
1139 generation, Atmos. Meas. Tech., 9, 1767–1784, https://doi.org/10.5194/amt-9-1767-2016, 2016.
1140

1141 Errera, Q., Y. Bennouna, M. Schulz, H.J. Eskes, S. Basart, A. Benedictow, A.-M. Blechschmidt, S.
1142 Chabrillat, H. Clark, E. Cuevas, H. Flentje, K.M. Hansen, U. Im, J. Kapsomenakis, B. Langerock, K.
1143 Petersen, A. Richter, N. Sudarchikova, V. Thouret, A. Wagner, Y. Wang, T. Warneke, C. Zerefos,
1144 Validation report of the CAMS global Reanalysis of aerosols and reactive gases, years 2003-2020,
1145 Copernicus Atmosphere Monitoring Service (CAMS) report, CAMS84_2018SC3_D5.1.1-2020.pdf,
1146 June 2021, doi:10.24380/8gf9-k005.

1147 European Space Agency (ESA): The four candidate Earth explorer core missions: Atmospheric
1148 dynamics mission, ESA Report for Mission Selection ESA SP, 1233, 145 pp., 1999
1149

1150 European Space Agency (ESA): ADM-Aeolus Science Report, ESA SP-1311, 121 pp., available at:
1151 https://earth.esa.int/documents/10174/1590943/AEOL002.pdf (last access: 14 June 2022), 2008.
1152

1153 European Space Agency (ESA): "ADM-Aeolus Mission Requirements Document", ESA EOP-
1154 SM/2047, 57 pp., available at: http://esamultimedia.esa.int/docs/EarthObservation/ADM-
1155 Aeolus_MRD.pdf (last access: 2 November 2019), 2016.
1156

1157 Fernald, F. G.: Analysis of atmospheric lidar observations: some comments, Appl. Opt., 23, 652–653,
1158 doi.org/10.1364/AO.23.000652, 1984.
1159

1160 Flamant, P., Dabas, A., Martinet, P., Lever, V., Flament, T., Trapon, D., Olivier, M., Cuesta, J., and
1161 Huber, D.: Aeolus L2A Algorithm Theoretical Baseline Document, Particle optical properties
1162 product, version 5.7, available at: https://earth.esa.int/eogateway/ catalog/aeolus-l2a-aerosol-cloud-
1163 optical-product (last access: 14 December 2021), 2021.
1164

1165 Flament, T., Trapon, D., Lacour, A., Dabas, A., Ehlers, F., and Huber, D.: Aeolus L2A aerosol optical
1166 properties product: standard correct algorithm and Mie correct algorithm, Atmos. Meas. Tech., 14,
1167 7851–7871, https://doi.org/10.5194/amt-14-7851-2021, 2021.
1168

1169 Fountoulakis, I., Papachristopoulou, K., Proestakis, E., Gkikas, A., Ioannis Raptis, P., Siomos, N.,

1170 Kontoes, C., and Kazadzis, S.: Effect of aerosol vertical distribution on the transfer of solar radiation

1171 through the atmosphere, EGU21-6111, https://doi.org/10.5194/egusphere-egu21-6111, 2021.

1172

1173 Freudenthaler, V.: About the effects of polarising optics on lidar signals and the Δ90 calibration,

1174 Atmos. Meas. Tech., 9, 4181–4255, https://doi.org/10.5194/amt-9-4181-2016, 2016.

1175

1176 Freudenthaler, V., Linné, H., Chaikovski, A., Rabus, D., Groß, S.: EARLINET lidar quality assurance

1177 tools, Atmos. Chem. Phys. Discuss., https://doi.org/10.5194/amt-2017-395, 2018.

1178

1179 Gelaro, R, McCarty, W., Suárez, M. J., Todling, R., Molod, A., Takacs, L., Randles, C. A., Darmenov,

1180 A., Bosilovich, M. G., Reichle, R., Wargan, K., Coy, L., Cullather, R., Draper, C., Akella, S.,

1181 Buchard, V., Conaty, A., da Silva, A. M., Gu, W., Kim, G., Koster, R., Lucchesi, R., Merkova, D.,

1182 Nielsen, J. E., Partyka, G., Pawson, S., Putman, W., Rienecker, M., Schubert, S. D., Sienkiewicz, M.,

1183 and Zhao, B.: The Modern-Era Retrospective Analysis for Research and Applications, Version 2

1184 (MERRA-2), J. Climate, 30, 5419–5454, https://doi.org/10.1175/JCLI-D-16-0758.1, 2017.

1185

1186 Gerasopoulos, E., Andreae, M. O., Zerefos, C. S., Andreae, T. W., Balis, D., Formenti, P., Merlet, P.,

1187 Amiridis, V., and Papastefanou, C.: Climatological aspects of aerosol optical properties in Northern

1188 Greece, Atmos. Chem. Phys., 3, 2025–2041, https://doi.org/10.5194/acp-3-2025-2003, 2003.

1189

1190 Gerasopoulos, E., Amiridis, V., Kazadzis, S., Kokkalis, P., Eleftheratos, K., Andreae, M. O., Andreae,

1191 T. W., El-Askary, H., and Zerefos, C. S.: Three-year ground based measurements of aerosol optical

1192 depth over the Eastern Mediterranean: the urban environment of Athens, Atmos. Chem. Phys., 11,

1193 2145–2159, https://doi.org/10.5194/acp-11-2145-2011, 2011.

1194

1195 Gialitaki, A., Tsekeri, A., Amiridis, V., Ceolato, R., Paulien, L., Kampouri, A., Gkikas, A., Solomos,

1196 S., Marinou, E., Haarig, M., Baars, H., Ansmann, A., Lapyonok, T., Lopatin, A., Dubovik, O., Groß,

1197 S., Wirth, M., Tsichla, M., Tsikoudi, I., and Balis, D.: Is the near-spherical shape the "new black" for

1198 smoke?, Atmos. Chem. Phys., 20, 14005–14021, https://doi.org/10.5194/acp-20-14005-2020, 2020.

1199

1200 Giles, D. M., Sinyuk, A., Sorokin, M. G., Schafer, J. S., Smirnov, A., Slutsker, I., Eck, T. F., Holben,

1201 B. N., Lewis, J. R., Campbell, J. R., Welton, E. J., Korkin, S. V., and Lyapustin, A. I.: Advancements

1202 in the Aerosol Robotic Network (AERONET) Version 3 database – automated near-real-time quality

control algorithm with improved cloud screening for Sun photometer aerosol optical depth (AOD) measurements, Atmos. Meas. Tech., 12, 169–209, https://doi.org/10.5194/amt-12-169-2019, 2019.

Gkikas, A., Hatzianastassiou, N., Mihalopoulos, N., Katsoulis, V., Kazadzis, S., Pey, J., Querol, X., and Torres, O.: The regime of intense desert dust episodes in the Mediterranean based on contemporary satellite observations and ground measurements, Atmos. Chem. Phys., 13, 12135–12154, https://doi.org/10.5194/acp-13-12135-2013, 2013.

Gkikas, A., Houssos, E. E., Lolis, C. J., Bartzokas, A., Mihalopoulos, N., and Hatzianastassiou, N.: Atmospheric circulation evolution related to desert-dust episodes over the Mediterranean, Q. J. Roy. Meteor. Soc., 141, 1634–1645, https://doi.org/10.1002/qj.2466, 2015.

Gkikas, A., Basart, S., Hatzianastassiou, N., Marinou, E., Amiridis, V., Kazadzis, S., Pey, J., Querol, X., Jorba, O., Gassó, S., and Baldasano, J. M.: Mediterranean intense desert dust outbreaks and their vertical structure based on remote sensing data, Atmos. Chem. Phys., 16, 8609–8642, https://doi.org/10.5194/acp-16-8609-2016, 2016.

Gkikas, A., Obiso, V., Pérez García-Pando, C., Jorba, O., Hatzianastassiou, N., Vendrell, L., Basart, S., Solomos, S., Gassó, S., and Baldasano, J. M.: Direct radiative effects during intense Mediterranean desert dust outbreaks, Atmos. Chem. Phys., 18, 8757–8787, https://doi.org/10.5194/acp-18-8757-2018, 2018.

Gkikas, A., Proestakis, E., Amiridis, V., Kazadzis, S., Di Tomaso, E., Marinou, E., Hatzianastassiou, N., Kok, J. F., and García-Pando, C. P.: Quantification of the dust optical depth across spatiotemporal scales with the MIDAS global dataset (2003–2017), Atmos. Chem. Phys., 22, 3553–3578, https://doi.org/10.5194/acp-22-3553-2022, 2022.

Gueymard, C. A. and Yang, D.: Worldwide validation of CAMS and MERRA-2 reanalysis aerosol optical depth products using 15 years of AERONET observations, Atmos. Environ., 225, 117216, https://doi.org/10.1016/j.atmosenv.2019.117216, 2020.

Haywood, J. M., Abel, S. J., Barrett, P. A., Bellouin, N., Blyth, A., Bower, K. N., Brooks, M., Carslaw, K., Che, H., Coe, H., Cotterell, M. I., Crawford, I., Cui, Z., Davies, N., Dingley, B., Field, P., Formenti, P., Gordon, H., de Graaf, M., Herbert, R., Johnson, B., Jones, A. C., Langridge, J. M.,

1237 Malavelle, F., Partridge, D. G., Peers, F., Redemann, J., Stier, P., Szpek, K., Taylor, J. W., Watson-
1238 Parris, D., Wood, R., Wu, H., and Zuidema, P.: The CLoud–Aerosol–Radiation Interaction and
1239 Forcing: Year 2017 (CLARIFY-2017) measurement campaign, Atmos. Chem. Phys., 21, 1049–1084,
1240 https://doi.org/10.5194/acp-21-1049-2021, 2021.

1242 Health Effects Institute, 2019, State of Global Air 2019, Special Report, Boston, MA: Health Effects
1243 Institute, ISSN 2578-6873,
1244 https://www.stateofglobalair.org/sites/default/files/soga_2019_report.pdf, 2019.

1246 Horányi, A., Cardinali, C., Rennie, M., and Isaksen, L.: The assimilation of horizontal line-of-sight
1247 wind information into the ECMWF data assimilation and forecasting system. Part I: The assessment
1248 of wind impact, Q. J. R. Meteorol. Soc., 141, 1223–1232, https://doi.org/10.1002/qj.2430, 2015a.

1250 Horányi, A., Cardinali, C., Rennie, M., and Isaksen, L.: The assimilation of horizontal line-of-sight
1251 wind information into the ECMWF data assimilation and forecasting system. Part II: The impact of
1252 degraded wind observations, Q. J. R. Meteorol. Soc., 141, 1233–1243,
1253 https://doi.org/10.1002/qj.2551, 2015b.

1255 Illingworth, A. J., Barker, H. W., Beljaars, A., Ceccaldi, M., Chepfer, H., Clerbaux, N., Cole, J.,
1256 Delanoë, J., Domenech, C., Donovan, D. P., Fukuda, S., Hirakata, M., Hogan, R. J., Huenerbein, A.,
1257 Kollias, P., Kubota, T., Nakajima, T., Nakajima, T. Y., Nishizawa, T., Ohno, Y., Okamoto, H., Oki,
1258 R., Sato, K., Satoh, M., Shephard, M. W., Velázquez-Blázquez, A., Wandinger, U., Wehr, T., and
1259 van Zadelhoff, G.-J.: The EarthCARE Satellite: The Next Step Forward in Global Measurements of
1260 Clouds, Aerosols, Precipitation, and Radiation, Bull. Amer. Meteor. Soc., 96, 1311–1332,
1261 https://doi.org/10.1175/BAMS-D-12-00227.1, 2015.

1263 Inness, A., Ades, M., Agustí-Panareda, A., Barré, J., Benedictow, A., Blechschmidt, A.-M.,
1264 Dominguez, J. J., Engelen, R., Eskes, H., Flemming, J., Huijnen, V., Jones, L., Kipling, Z., Massart,
1265 S., Parrington, M., Peuch, V.-H., Razinger, M., Remy, S., Schulz, M., and Suttie, M.: The CAMS
1266 reanalysis of atmospheric composition, Atmos. Chem. Phys., 19, 3515–3556,
1267 https://doi.org/10.5194/acp-19-3515-2019, 2019.

1269 Isaksen, L. and Rennie, M.: A preliminary evaluation of using Aeolus L2B Winds in ECMWF's NWP
1270 system, with focus on the tropical region, in: ESA Living Planet Symposium 2019, Milan, Italy,

https://lps19.esa.int/NikalWebsitePortal/living-planet-symposium-2019/lps19/Agenda/AgendaItemDetail?id=64570099-bea7-4b8f-a54b-5b6ad81fa342, last access: 8 May 2020, 2019.

Jickells, T. D., An, Z. S., Andersen, K. K., Baker, A. R., Bergametti, G., Brooks, N., Cao, J. J., Boyd, P. W., Duce, R. A., Hunter, K. A., Kawahata, H., Kubilay, N., laRoche, J., Liss, P. S., Mahowald, N., Prospero, J. M., Ridgwell, A. J., Tegen, I. and Torres, R.: Global Iron Connections Between Desert Dust, Ocean Biogeochemistry, and Climate, Science, 308(5718), 67–71, doi:10.1126/science.1105959, 2005.

Kampouri, A., Amiridis, V., Solomos, S., Gialitaki, A., Marinou, E., Spyrou, C., Georgoulias, A. K., Akritidis, D., Papagiannopoulos, N., Mona, L., Scollo, S., Tsichla, M., Tsikoudi, I., Pytharoulis, I., Karacostas, T., and Zanis, P.: Investigation of Volcanic Emissions in the Mediterranean: "The Etna–Antikythera Connection," 12, 40, https://doi.org/10.3390/atmos12010040, 2021.

Kanakidou, M., Mihalopoulos, N., Kindap, T., Im, U., Vrekoussis, M., Gerasopoulos, E., Dermitzaki, E., Unal, A., Kocak, M., Markakis, K., Melas, D., Kouvarakis, G., Youssef, A. F., Richter, A., Hatzianastassiou, N., Hilboll, A., Ebojie, F., Wittrock, F., von Savigny, C., Burrows, J. P., Ladstaetter-Weissenmayer, A., and Moubasher, H.: Megacities as hot spots of air pollution in the East Mediterranean, Atmos. Environ., 45, 1223–1235, https://doi.org/10.1016/j.atmosenv.2010.11.048, 2011.

Kanitz, T., Lochard, J., Marshall, J., McGoldrick, P., Lecrenier, O., Bravetti, P., Reitebuch, O., Rennie, M., Wernham, D., and Elfving, A.: Aeolus first light: first glimpse, in: International Conference on Space Optics – ICSO 2018, 9–12 October 2018, Chania, Greece, vol. 11180, 659–664, https://doi.org/10.1117/12.2535982, 2019.

Klett, J. D.: Stable analytical inversion solution for processing lidar returns, Appl. Optics, 20, 211–220, https://doi.org/10.1364/AO.20.000211, 1981.

Kosmopoulos, P. G., Kazadzis, S., El-Askary, H., Taylor, M., Gkikas, A., Proestakis, E., Kontoes, C. and El-Khayat, M. M.: Earth-Observation-Based Estimation and Forecasting of Particulate Matter Impact on Solar Energy in Egypt, Remote Sens., 10(12), 1870, doi:10.3390/rs10121870, 2018.

1305 Kosmopoulos, P.G., Kazadzis, S., Taylor, M., Raptis, P.I., Keramitsoglou, I., Kiranoudis, C., and
1306 Bais, A.F.: Assessment of the surface solar irradiance derived from real-time modelling techniques
1307 and verification with ground-based measurements. Atmos. Meas. Tech., 11, pp 907-924, DOI:
1308 10.5194/amt-11-907-2018, 2018.

1309

1310 Lee, L., Zhang, J., Reid, J. S., and Yorks, J. E.: Investigation of CATS aerosol products and
1311 application toward global diurnal variation of aerosols, Atmos. Chem. Phys., 19, 12687–12707,
1312 https://doi.org/10.5194/acp-19-12687-2019, 2019.

1313

1314 Lelieveld, J., Berresheim, H., Borrmann, S., Crutzen, P. J., Dentener, F. J., Fischer, H., Feichter, J.,
1315 Flatau, P. J., Heland, J., Holzinger, R., Korrmann, R., Lawrence, M. G., Levin, Z., Markowicz, K.
1316 M., Mihalopoulos, N., Minikin, A., Ramanathan, V., de Reus, M., Roelofs, G. J., Scheeren, H. A.,
1317 Sciare, J., Schlager, H., Schultz, M., Siegmund, P., Steil, B., Stephanou, E. G., Stier, P., Traub, M.,
1318 Warneke, C., Williams, J., and Ziereis, H.: Global Air Pollution Crossroads over the Mediterranean,
1319 Science, 298, 794–799, https://doi.org/10.1126/science.1075457, 2002.

1320

1321 Lelieveld, J., Evans, J. S., Fnais, M., Giannadaki, D., and Pozzer, A.: The contribution of outdoor air
1322 pollution sources to premature mortality on a global scale, Nature, 525, 367–371,
1323 https://doi.org/10.1038/nature15371, 2015.

1324

1325 Levy, R. C., Mattoo, S., Munchak, L. A., Remer, L. A., Sayer, A. M., Patadia, F., and Hsu, N. C.:
1326 The Collection 6 MODIS aerosol products over land and ocean, Atmos. Meas. Tech., 6, 2989–3034,
1327 https://doi.org/10.5194/amt-6-2989-2013, 2013.

1328

1329 Li, W., El-Askary, H., Qurban, M. A., Proestakis, E., Garay, M. J., Kalashnikova, O. V., Amiridis,
1330 V., Gkikas, A., Marinou, E., Piechota, T., and Manikandan, K. P.: An Assessment of Atmospheric
1331 and Meteorological Factors Regulating Red Sea Phytoplankton Growth, Remote Sens., 10, 673,
1332 https://doi.org/10.3390/rs10050673, 2018.

1333

1334 Li, J., Carlson, B.E., Yung, Y.L. et al. Scattering and absorbing aerosols in the climate system. Nat
1335 Rev Earth Environ 3, 363–379 (2022). https://doi.org/10.1038/s43017-022-00296-7

1336

Liu, D., Wang, Z., Liu, Z., Winker, D., and Trepte, C.: A height resolved global view of dust aerosols from the first year CALIPSO lidar measurements, J. Geophys. Res.-Atmos., 113, D16214, https://doi.org/10.1029/2007JD009776, 2008.

Liu, Z., Kar, J., Zeng, S., Tackett, J., Vaughan, M., Avery, M., Pelon, J., Getzewich, B., Lee, K.-P., Magill, B., Omar, A., Lucker, P., Trepte, C., and Winker, D.: Discriminating between clouds and aerosols in the CALIOP version 4.1 data products, Atmos. Meas. Tech., 12, 703–734, https://doi.org/10.5194/amt-12-703-2019, 2019.

Lux, O., Lemmerz, C., Weiler, F., Marksteiner, U., Witschas, B., Rahm, S., Geiß, A., and Reitebuch, O.: Intercomparison of wind observations from the European Space Agency's Aeolus satellite mission and the ALADIN Airborne Demonstrator, Atmos. Meas. Tech., 13, 2075–2097, https://doi.org/10.5194/amt-13-2075-2020, 2020.

Lux, O., Lemmerz, C., Weiler, F., Marksteiner, U., Witschas, B., Rahm, S., Geiß, A., Schäfler, A., and Reitebuch, O.: Retrieval improvements for the ALADIN Airborne Demonstrator in support of the Aeolus wind product validation, Atmos. Meas. Tech., 15, 1303–1331, https://doi.org/10.5194/amt-15-1303-2022, 2022.

Mallios, S. A., Daskalopoulou, V., and Amiridis, V.: Orientation of non spherical prolate dust particles moving vertically in the Earth's atmosphere, J. Aerosol Sci., 151, 105657, doi:https://doi.org/10.1016/j.jaerosci.2020.105657, 2021.

Marinou, E., Amiridis, V., Binietoglou, I., Tsikerdekis, A., Solomos, S., Proestakis, E., Konsta, D., Papagiannopoulos, N., Tsekeri, A., Vlastou, G., Zanis, P., Balis, D., Wandinger, U. and Ansmann, A.: Three-dimensional evolution of Saharan dust transport towards Europe based on a 9-year EARLINET-optimized CALIPSO dataset, Atmos. Chem. Phys., 17(9), 5893–5919, doi:10.5194/acp-17-5893-2017, 2017.

Martin, A., Weissmann, M., Reitebuch, O., Rennie, M., Geiß, A., and Cress, A.: Validation of Aeolus winds using radiosonde observations and numerical weather prediction model equivalents, Atmos. Meas. Tech., 14, 2167–2183, https://doi.org/10.5194/amt-14-2167-2021, 2021.

1370 Matthias, V., Freudenthaler, V., Amodeo, A., Balin, I., Balis, D., Bösenberg, J., Chaikovsky, A.,
1371 Chourdakis, G., Comeron, A., Delaval, A., De Tomasi, F., Eixmann, R., Hågård, A., Komguem, L.,
1372 Kreipl, S., Matthey, R., Rizi, V., Rodrigues, J., Wandinger, U., and Wang, X.: Aerosol lidar
1373 intercomparison in the framework of the EARLINET project. 1. Instruments, Appl. Opt., 43, 961-
1374 976, doi:10.1364/AO.43.000961, 2004.

1375

1376 Mattis, I., D'Amico, G., Baars, H., Amodeo, A., Madonna, F., and Iarlori, M.: EARLINET Single
1377 Calculus Chain – technical – Part 2: Calculation of optical products, Atmos. Meas. Tech., 9, 3009–
1378 3029, https://doi.org/10.5194/amt-9-3009-2016, 2016.

1379

1380 McGill, M. J., Yorks, J. E., Scott, V. S., Kupchock, A. W., and Selmer, P. A.: The Cloud Aerosol
1381 Transport System (CATS): A technology demonstration on the International Space Station, Proc.
1382 SPIE 9612, Lidar Remote Sensing for Environmental Monitoring XV, 96120A,
1383 https://doi.org/10.1117/12.2190841, 2015.

1384

1385 MétéoFrance: Algorithm theoretical basis document for cloud products (CMa-PGE01   v3.2, CT-
1386 PGE02 v2.2 & CTTH-PGE03 v2.2), Technical Report   SAF/NWC/CDOP/MFL/SCI/ATBD/01,
1387 Paris: MétéoFrance, 2013.

1388

1389 Middleton, N., Tozer, P., and Tozer, B.: Sand and dust storms: underrated natural hazards, Disasters,
1390 43, 390–409, https://doi.org/10.1111/disa.12320, 2018.

1391

1392 Mishchenko, M. I. and Hovenier, J. W.: Depolarization of light backscattered by randomly oriented
1393 nonspherical particles, Opt. Lett., 20(12), 1356, doi:10.1364/OL.20.001356, 1995.

1394

1395 Müller, D., Ansmann, A., Mattis, I., Tesche, M., Wandinger, U., Althausen, D., & Pisani, G. (2007).
1396 Aerosol-type-dependent lidar ratios observed with raman lidar. Journal of Geophysical Research
1397 Atmospheres, 112(16) doi:10.1029/2006JD008292

1398

1399 Okin, G. S., Mahowald, N., Chadwick, O. A. and Artaxo, P.: Impact of desert dust on the
1400 biogeochemistry of phosphorus in terrestrial ecosystems, Global Biogeochemical Cycles, 18(2),
1401 doi:10.1029/2003GB002145, 2004.

1402

O'Neill, N. T., Eck, T. F., Smirnov, A., Holben, B. N., and Thulasiraman, S.: Spectral discrimination of coarse and fine mode optical depth, J. Geophys. Res., 108, 4559–4573, https://doi.org/10.1029/2002JD002975, 2003.

Papagiannopoulos, N., D'Amico, G., Gialitaki, A., Ajtai, N., Alados-Arboledas, L., Amodeo, A., Amiridis, V., Baars, H., Balis, D., Binietoglou, I., Comerón, A., Dionisi, D., Falconieri, A., Fréville, P., Kampouri, A., Mattis, I., Mijić, Z., Molero, F., Papayannis, A., Pappalardo, G., Rodríguez-Gómez, A., Solomos, S. and Mona, L.: An EARLINET early warning system for atmospheric aerosol aviation hazards, Atmospheric Chemistry and Physics, 20(18), 10775–10789, doi:https://doi.org/10.5194/acp-20-10775-2020, 2020.

Pappalardo, G., Amodeo, A., Apituley, A., Comeron, A., Freudenthaler, V., Linné, H., Ansmann, A., Bösenberg, J., D'Amico, G., Mattis, I., Mona, L., Wandinger, U., Amiridis, V., Alados-Arboledas, L., Nicolae, D., and Wiegner, M.: EARLINET: towards an advanced sustainable European aerosol lidar network, Atmos. Meas. Tech., 7, 2389–2409, https://doi.org/10.5194/amt-7-2389-2014, 2014.

Papayannis, A., Balis, D., Amiridis, V., Chourdakis, G., Tsaknakis, G., Zerefos, C., Castanho, A. D. A., Nickovic, S., Kazadzis, S., and Grabowski, J.: Measurements of Saharan dust aerosols over the Eastern Mediterranean using elastic backscatter-Raman lidar, spectrophotometric and satellite observations in the frame of the EARLINET project, Atmos. Chem. Phys., 5, 2065–2079, https://doi.org/10.5194/acp-5-2065-2005, 2005.

Paschou, P., Siomos, N., Tsekeri, A., Louridas, A., Georgoussis, G., Freudenthaler, V., Binietoglou, I., Tsaknakis, G., Tavernarakis, A., Evangelatos, C., von Bismarck, J., Kanitz, T., Meleti, C., Marinou, E., and Amiridis, V.: The eVe reference polarisation lidar system for the calibration and validation of the Aeolus L2A product, Atmos. Meas. Tech., 15, 2299–2323, https://doi.org/10.5194/amt-15-2299-2022, 2022.

Pappalardo, G., Wandinger, U., Mona, L., Hiebsch, A., Mattis, I., Amodeo, A., Ansmann, A., Seifert, P., Linne, H., Apituley, A., Alados Arboledas, L., Balis, D., Chaikovsky, A., D'Amico, G., De Tomasi, F., Freudenthaler, V., Giannakaki, E., Giunta, A., Grigorov, I., Iarlori, M., Madonna, F., Mamouri, R.-E., Nasti, L., Papayannis, A., Pietruczuk, A., Pujadas, M., Rizi, V., Rocadenbosch, F., Russo, F., Schnell, F., Spinelli, N., Wang, X., and Wiegner, M.: EARLINET correlative

measurements for CALIPSO: First intercomparison results, J. Geophys. Res., 115, D00H19, doi:10.1029/2009JD012147, 2010.

Pappalardo, G., Amodeo, A., Apituley, A., Comeron, A., Freudenthaler, V., Linné, H., Ansmann, A., Bösenberg, J., D'Amico, G., Mattis, I., Mona, L., Wandinger, U., Amiridis, V., Alados-Arboledas, L., Nicolae, D., and Wiegner, M.: EARLINET: towards an advanced sustainable European aerosol lidar network, Atmos. Meas. Tech., 7, 2389–2409, https://doi.org/10.5194/amt-7-2389-2014, 2014.

Pérez, C., Nickovic, S., Pejanovic, G., Baldasano, J. M., and Özsoy, E.: Interactive dust-radiation modeling: A step to improve weather forecasts, J. Geophys. Res., 111, 1–17, 2006.

Pisso, I., Sollum, E., Grythe, H., Kristiansen, N.I., Cassiani, M., Eckhardt, S., Arnold, D., Morton, D., Thompson, R.L., Groot Zwaaftink, C.D., Evangeliou, N., Sodemann, H., Haimberger, L., Henne, S., Brunner, D., Burkhart, J.F., Fouilloux, A., Brioude, J., Philipp, A., Seibert, P., and Stohl, A.: FLEXPART 10.4 (Version 10.4), Geosci. Model Dev. Discuss. Zenodo, https://doi.org/10.5281/zenodo.3542278, 2019.

Pöschl, U.: Atmospheric Aerosols: Composition, Transformation, Climate and Health Effects, ANGEW CHEM INT EDIT, 44, 7520-7540, 10.1002/anie.200501122, 2005.

Proestakis, E., Amiridis, V., Marinou, E., Georgoulias, A. K., Solomos, S., Kazadzis, S., Chimot, J., Che, H., Alexandri, G., Binietoglou, I., Daskalopoulou, V., Kourtidis, K. A., de Leeuw, G. and Ronald, J. van der A.: Nine-year spatial and temporal evolution of desert dust aerosols over South and East Asia as revealed by CALIOP, Atmos. Chem. Phys., 18(2), 1337–1362, doi:10.5194/acp-18-1337-2018, 2018.

Proestakis, E., Amiridis, V., Marinou, E., Binietoglou, I., Ansmann, A., Wandinger, U., Hofer, J., Yorks, J., Nowottnick, E., Makhmudov, A., Papayannis, A., Pietruczuk, A., Gialitaki, A., Apituley, A., Szkop, A., Muñoz Porcar, C., Bortoli, D., Dionisi, D., Althausen, D., Mamali, D., Balis, D., Nicolae, D., Tetoni, E., Liberti, G. L., Baars, H., Mattis, I., Stachlewska, I. S., Voudouri, K. A., Mona, L., Mylonaki, M., Perrone, M. R., Costa, M. J., Sicard, M., Papagiannopoulos, N., Siomos, N., Burlizzi, P., Pauly, R., Engelmann, R., Abdullaev, S., and Pappalardo, G.: EARLINET evaluation of the CATS Level 2 aerosol backscatter coefficient product, Atmos. Chem. Phys., 19, 11743–11764, https://doi.org/10.5194/acp-19-11743-2019, 2019.

1470

Pye, H.O.T., Ward-Caviness, C.K., Murphy, B.N. et al. Secondary organic aerosol association with cardiorespiratory disease mortality in the United States. Nat Commun 12, 7215 (2021). https://doi.org/10.1038/s41467-021-27484-1

Randles, C. A., da Silva, A. M., Buchard, V., Colarco, P. R., Darmenov, A., Govindaraju, R., Smirnov, A., Holben, B., Ferrare, R., Hair, J., Shinozuka, Y., Flynn, C. J., Randles, C. A., Silva, A. M. da, Buchard, V., Colarco, P. R., Darmenov, A., Govindaraju, R., Smirnov, A., Holben, B., Ferrare, R., Hair, J., Shinozuka, Y., and Flynn, C. J.: The MERRA-2 Aerosol Reanalysis, 1980 Onward. Part I: System Description and Data Assimilation Evaluation, J. Climate, 30, 6823–6850, https://doi.org/10.1175/JCLI-D-16-0609.1, 2017.

Reitebuch, O., Lemmerz, C., Lux, O., Marksteiner, U., Rahm, S., Weiler, F., Witschas, B., Meringer, M., Schmidt, K., Huber, D., Nikolaus, I., Geiss, A., Vaughan, M., Dabas, A., Flament, T., Stieglitz, H., Isaksen, L., Rennie, M., de Kloe, J., Marseille, G.-J., Stoffelen, A., Wernham, D., Kanitz, T., Straume, A.-G., Fehr, T., von Bismarck, J., Floberghagen, R., and Par- rinello, T.: Initial Assessment of the Performance of the First Wind Lidar in Space on Aeolus, EPJ Web Conf., 237, 01010, https://doi.org/10.1051/epjconf/202023701010, 2020.

Remer, L. A., Kleidman, R. G., Levy, R. C., Kaufman, Y. J., Tanré, D., Mattoo, S., Martins, J. V., Ichoku, C., Koren, I., Yu, H. and Holben, B. N.: Global aerosol climatology from the MODIS satellite sensors, J. Geophys. Res.-Atmos., 113, D14S07, https://doi.org/10.1029/2007JD009661, 2008.

Rennie, M. P. and Isaksen, L.: Investigations Into the Quality of Aeolus L2B Winds Using the ECMWF Model and Initial NWP Impact Assessment, in: ESA Living Planet Symposium 2019, Milan, Italy, https://lps19.esa.int/NikalWebsitePortal/living-planet-symposium-2019/lps19/Agenda/AgendaItemDetail?id=1a3d272c-f7d1-4847-b1c4-08c452f9405f, last access: 8 May 2020, 2019.

Rennie, M. P., Isaksen, L., Weiler, F., de Kloe, J., Kanitz, T., and Reitebuch, O.: The impact of Aeolus wind retrievals on ECMWF global weather forecasts, Q. J. Roy. Meteor. Soc., 147, 3555–3586, https://doi.org/10.1002/qj.4142, 2021.

1502

Richardson, S. C., Mytilinaios, M., Foskinis, R., Kyrou, C., Papayannis, A., Pyrri, I., Giannoutsou, E., and Adamakis, I. D. S.: Bioaerosol detection over Athens, Greece using the laser induced fluorescence technique, Sci. Total Environ., 696, 133906, https://doi.org/10.1016/j.scitotenv.2019.133906, 2019.

Roebeling, R. A., Feijt, A. J., and Stamnes, P.: Cloud property retrievals for climate monitoring: implications of differences between SEVIRI on METEOSAT-8 and AVHRR on NOAA-17, J. Geophys. Res., 111, 20210,   https://doi.org/10.1029/2005JD006990, 2006.

Roy, G. and Roy, N.: Relation between circular and linear depolarization ratios under multiple-scattering conditions, Appl. Opt., doi:10.1364/ao.47.006563, 2008.

Sasano, Y. and Nakane, H.: Significance of the extinction/backscatter ratio and the boundary value term in the solution for the two-component lidar equation, Appl. Opt., 23(1), 11_1--13, doi:10.1364/AO.23.0011_1, 1984.

Sayer, A. M., Hsu, N. C., Bettenhausen, C., and Jeong, M.-J.: Validation and uncertainty estimates for MODIS Collection 6 "Deep Blue" aerosol data, J. Geophys. Res., 118, 7864–7873, https://doi.org/10.1002/jgrd.50600, 2013.

Schmetz, J., Pili, P., Tjemkes, S., Just, D., Kerkmann, J., Rota, S., and Ratier, A.: An introduction to Meteosat Second Generation (MSG), B. Am. Meteorol. Soc., 83, 977–992, https://doi.org/10.1175/1520-0477(2002)083<0977:AITMSG>2.3.CO;2, 2002.

Shinozuka, Y. and Redemann, J.: Horizontal variability of aerosol optical depth observed during the ARCTAS airborne experiment, Atmos. Chem. Phys., 11, 8489–8495, https://doi.org/10.5194/acp-11-8489-2011, 2011.

Sinyuk, A., Holben, B. N., Eck, T. F., Giles, D. M., Slutsker, I., Korkin, S., Schafer, J. S., Smirnov, A., Sorokin, M., and Lyapustin, A.: The AERONET Version 3 aerosol retrieval algorithm, associated uncertainties and comparisons to Version 2, Atmos. Meas. Tech., 13, 3375–3411, https://doi.org/10.5194/amt-13-3375-2020, 2020.

1536 Siomos, N., Balis, D. S., Voudouri, K. A., Giannakaki, E., Filioglou, M., Amiridis, V., Papayannis,
1537 A., and Fragkos, K.: Are EARLINET and AERONET climatologies consistent? The case of
1538 Thessaloniki, Greece, Atmos. Chem. Phys., 18, 11885–11903, https://doi.org/10.5194/acp-18-11885-
1539 2018, 2018.

1541 Solomon S., Dube K., Stone K., Yu P., Kinnison D., Toon O.B., Strahan S.E., Rosenlof K.H.,
1542 Portmann R., Davis S., Randel W., Bernath P., Boone C., Bardeen C.G., Bourassa A., Zawada D.,
1543 Degenstein D.: On the stratospheric chemistry of midlatitude wildfire smoke (2022) Proceedings of
1544 the National Academy of Sciences of the United States of America, 119 (10), pp. e2117325119 DOI:
1545 10.1073/pnas.2117325119

1547 Stoffelen, A., Pailleux, J., Källén, E., Vaughan, J. M., Isaksen, L., Flamant, P., Wergen, W.,
1548 Andersson, E., Schyberg, H., Culoma, A., Meynart, R., Endemann, M., and Ingmann, P.: The
1549 atmospheric dynamics mission for global wind field measurement, B. Am. Meteorol. Soc., 86, 73-87,
1550 https://doi.org/10.1175/BAMS-86-1-73, 2005.

1552 Stohl, A., Forster, C., Frank, A., Seibert, P., and Wotawa, G.: Technical note: The Lagrangian particle
1553 dispersion model FLEXPART version 6.2, Atmos. Chem. Phys., 5, 2461–2474, doi:10.5194/acp-5-
1554 2461-2005, 2005.

1556 Straume, A.G., Schuettemeyer, D., von Bismarck, J., Kanitz, T., Fehr, T., EOP-SM/2945/AGS-ags,
1557 PL-Plan, European Space Agency (ESA),
1558 https://earth.esa.int/eogateway/documents/20142/1564626/Aeolus-Scientific-CAL-VAL-
1559 Implementation-Plan.pdf, 2019.

1561 Straume, A. G., Rennie, M., Isaksen, L., de Kloe, J., Marseille, G.-J., Stoffelen, A., Flament, T.,
1562 Stieglitz, H., Dabas, A., Huber, D., Reitebuch, O., Lemmerz, C., Lux, O., Marksteiner, U., Weiler,
1563 F., Witschas, B., Meringer, M., Schmidt, K., Nikolaus, I., Geiß, A., Flamant, P., Kanitz, T., Wernham,
1564 D., von Bismarck, J., Bley, S., Fehr, T., Floberghagen, R., and Parrinello, T.: ESA's space-based
1565 Doppler wind lidar mission Aeolus – First wind and aerosol product assessment results, EPJ Web
1566 Conf., 237, 01007, https://doi.org/10.1051/epjconf/202023701007, 2020.

1568 Tyrlis, E. and Lelieveld, J.: Climatology and Dynamics of the Summer Etesian Winds over the
1569 Eastern Mediterranean, J. Atmos. Sci., 70, 3374–3396, 2013.

1570

van der Werf, G. R., Randerson, J. T., Giglio, L., van Leeuwen, T. T., Chen, Y., Rogers, B. M., Mu, M., van Marle, M. J. E., Morton, D. C., Collatz, G. J., Yokelson, R. J., and Kasibhatla, P. S.: Global fire emissions estimates during 1997–2016, Earth Syst. Sci. Data, 9, 697–720, https://doi.org/10.5194/essd-9-697-2017, 2017.

Ulanowski, Z., Bailey, J., Lucas, P. W., Hough, J. H., and Hirst, E.: Alignment of atmospheric mineral dust due to electric field, Atmos. Chem. Phys., 7, 6161–6173, https://doi.org/10.5194/acp-7-6161-2007, 2007.

Varlas, G.; Marinou, E.; Gialitaki, A.; Siomos, N.; Tsarpalis, K.; Kalivitis, N.; Solomos, S.; Tsekeri, A.; Spyrou, C.; Tsichla, M.; Kampouri, A.; Vervatis, V.; Giannakaki, E.; Amiridis, V.; Mihalopoulos, N.; Papadopoulos, A.; Katsafados, P. Assessing Sea-State Effects on Sea-Salt Aerosol Modeling in the Lower Atmosphere Using Lidar and In-Situ Measurements. Remote Sens., 13, 614. https://doi.org/10.3390/rs13040614, 2021.

Voudouri, K.A., Siomos, N., Michailidis, K., D'Amico, G., Mattis, I., Balis, D.: Consistency of the Single Calculus Chain optical products with archived measurements from an EARLINET lidar station, Remote Sensing. 2020; 12(23):3969. https://doi.org/10.3390/rs12233969, 2020.

Wei, J., Li, Z., Peng, Y., and Sun, L.: MODIS Collection 6.1 aerosol optical depth products over land and ocean: validation and comparison, Atmos. Environ., 201, 428–440, 2019

Weiler, F., Rennie, M., Kanitz, T., Isaksen, L., Checa, E., de Kloe, J., Okunde, N., and Reitebuch, O.: Correction of wind bias for the lidar on board Aeolus using telescope temperatures, At- mos. Meas. Tech., 14, 7167–7185, https://doi.org/10.5194/amt- 14-7167-2021, 2021.

Weinzierl, B., Ansmann, A., Prospero, J. M., Althausen, D., Benker, N., Chouza, F., Dollner, M., Farrell, D., Fomba, W. K., Freudenthaler, V., Gasteiger, J., Groß, S., Haarig, M., Heinold, B., Kandler, K., Kristensen, T. B., Mayol-Bracero, O. L., Müller, T., Reitebuch, O., Sauer, D., Schäfler, A., Schepanski, K., Spanu, A., Tegen, I., Toledano, C. and Walser, A.: The Saharan Aerosol Long-Range Transport and Aerosol–Cloud-Interaction Experiment: Overview and Selected Highlights, Bull. Amer. Meteor. Soc., 98(7), 1427–1451, doi:10.1175/BAMS-D-15-00142.1, 2016.

1603

Wilks, D.S. Statistical Methods in the Atmospheric Sciences, 4th ed.; Elsevier: Cambridge, MA, USA, 2019.

Winker, D. M., Vaughan, M. A., Omar, A., Hu, Y., Powell, K. A., Liu, Z., Hunt, W. H. and Young, S. A.: Overview of the CALIPSO Mission and CALIOP Data Processing Algorithms, J. Atmos. Ocean. Technol., 26(11), 2310–2323, doi:10.1175/2009JTECHA1281.1, 2009.

Witschas, B., Lemmerz, C., Geiß, A., Lux, O., Marksteiner, U., Rahm, S., Reitebuch, O., and Weiler, F.: First validation of Aeolus wind observations by airborne Doppler wind lidar measurements, Atmos. Meas. Tech., 13, 2381–2396, https://doi.org/10.5194/amt-13-2381-2020, 2020.

Witschas, B., Lemmerz, C., Lux, O., Marksteiner, U., Reitebuch, O., Weiler, F., Fabre, F., Dabas, A., Flament, T., Huber, D., and Vaughan, M.: Spectral performance analysis of the Aeolus Fabry–Pérot and Fizeau interferometers during the first years of operation, Atmos. Meas. Tech., 15, 1465–1489, https://doi.org/10.5194/amt-15-1465-2022, 2022.

Zeng, S., Vaughan, M., Liu, Z., Trepte, C., Kar, J., Omar, A., Winker, D., Lucker, P., Hu, Y., Getzewich, B., and Avery, M.: Application of high-dimensional fuzzy k-means cluster analysis to CALIOP/CALIPSO version 4.1 cloud–aerosol discrimination, Atmos. Meas. Tech., 12, 2261–2285, https://doi.org/10.5194/amt-12-2261-2019, 2019.

Zerefos, C., Nastos, P., Balis, D., Papayannis, A., Kelepertsis, A., Kannelopoulou, E., Nikolakis, D., Eleftheratos, C., Thomas, W., and Varotsos, C.: A complex study of Etna's volcanic plume from ground-based, in situ and space-borne observations, International J. Remote Sens., 27, 1855–1864, https://doi.org/10.1080/01431160500462154, 2006.

Table 1: Statistical metrics for the unfiltered (clouds plus aerosols) Aeolus L2A SCA and SCA mid-bin backscatter (in $Mm^{-1}sr^{-1}$) profiles at each PANACEA site.

Station	SCA					SCA_mid_bin				
	Counts	Bias	Rel. Bias (%)	R	RMSE	Counts	Bias	Rel. Bias (%)	R	RMSE
ANT	255	0.06	13.63	0.49	1.14	173	0.25	45.59	0.57	1.01
ATH	60	0.73	199.65	0.49	2.26	43	1.16	272.84	0.52	3.10
THE	222	0.83	185.16	0.34	2.60	140	1.10	224.65	0.32	2.19

Table 2: As in Table 1 but for the filtered (only aerosols) Aeolus backscatter retrievals (in $Mm^{-1}sr^{-1}$).

Station	SCA					SCA_mid_bin				
	Counts	Bias	Rel. Bias (%)	R	RMSE	Counts	Bias	Rel. Bias (%)	R	RMSE
ANT	94	-0.10	-26.57	0.55	0.78	57	0.06	13.35	0.86	0.43
ATH	12	1.08	483.36	0.75	3.33	9	0.73	312.67	0.82	1.41
THE	133	0.46	130.49	0.39	1.86	81	0.55	145.08	0.43	1.20
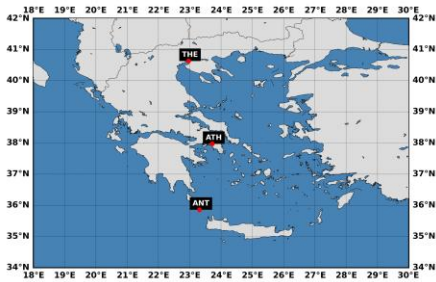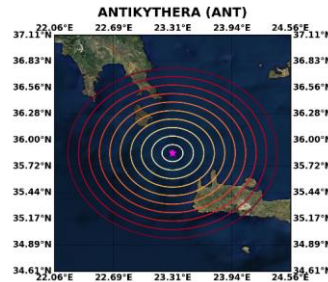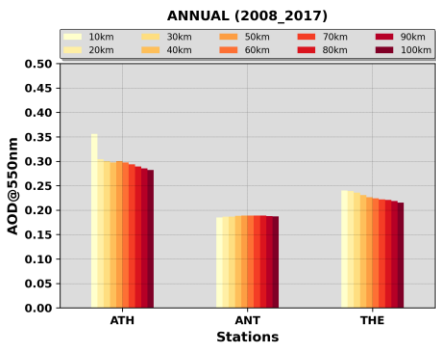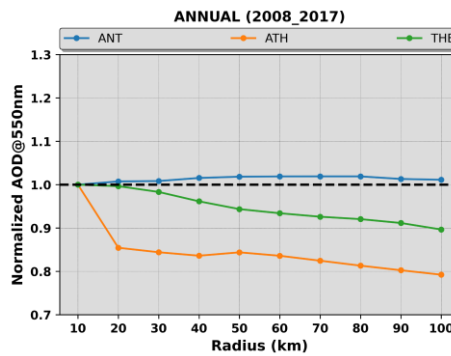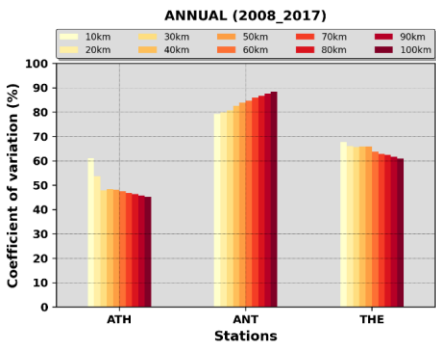
1664   **Figure 1:** (i) Locations of the three Greek PANACEA sites, namely Athens (ATH), Antikythera (ANT) and Thessaloniki
1665   (THE), (ii) Concentric circles, around the Antikythera island, of radii from 10 to 100 km with an incremental step of 10
1666   km, (iii) Climatological MODIS-Aqua AOD levels, representative for the period 2008 – 2017, for each circle area centered
1667   at each PANACEA site, (iv) Normalized climatological AODs for each circle area with respect to the corresponding

1668 levels of the inner circle, (v) Coefficient of variation (CV; expressed in percentage) of MODIS-Aqua AOD, representative
1669 for the period 2008 – 2017, for each circle area centered at each PANACEA site.

(i) **(ii)** **(iii)**
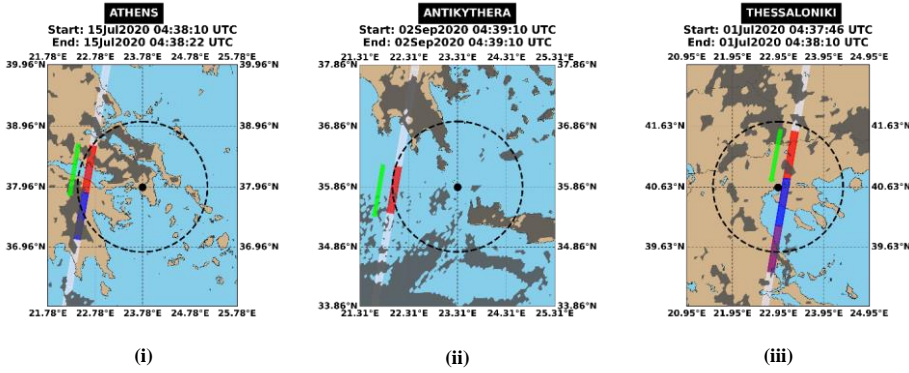
1670 **Figure 2:** The white stripe indicates the ALADIN's measurements track and the colored rectangles correspond to the
1671 Aeolus observations (~90 km along-track averaged measurements) falling within a radius of 120 km (dashed black line)
1672 of the PANACEA stations (black dot). The green arrows show the Aeolus flight directions (descending orbits for these
1673 examples). Dark grey shaded areas: MSG-SEVIRI cloud mask product (CLM) at the nearest time to Aeolus overpass.
1674 The start and end time (in UTC) of the ALADIN observations are given in the title of each plot.

1675
1676
1677
1678
1679
1680
1681
1682
1683
1684
1685
1686
1687
1688
1689
1690
1691
1692
1693
1694
1695

Deleted: orange

Deleted: s

Deleted: ascending or
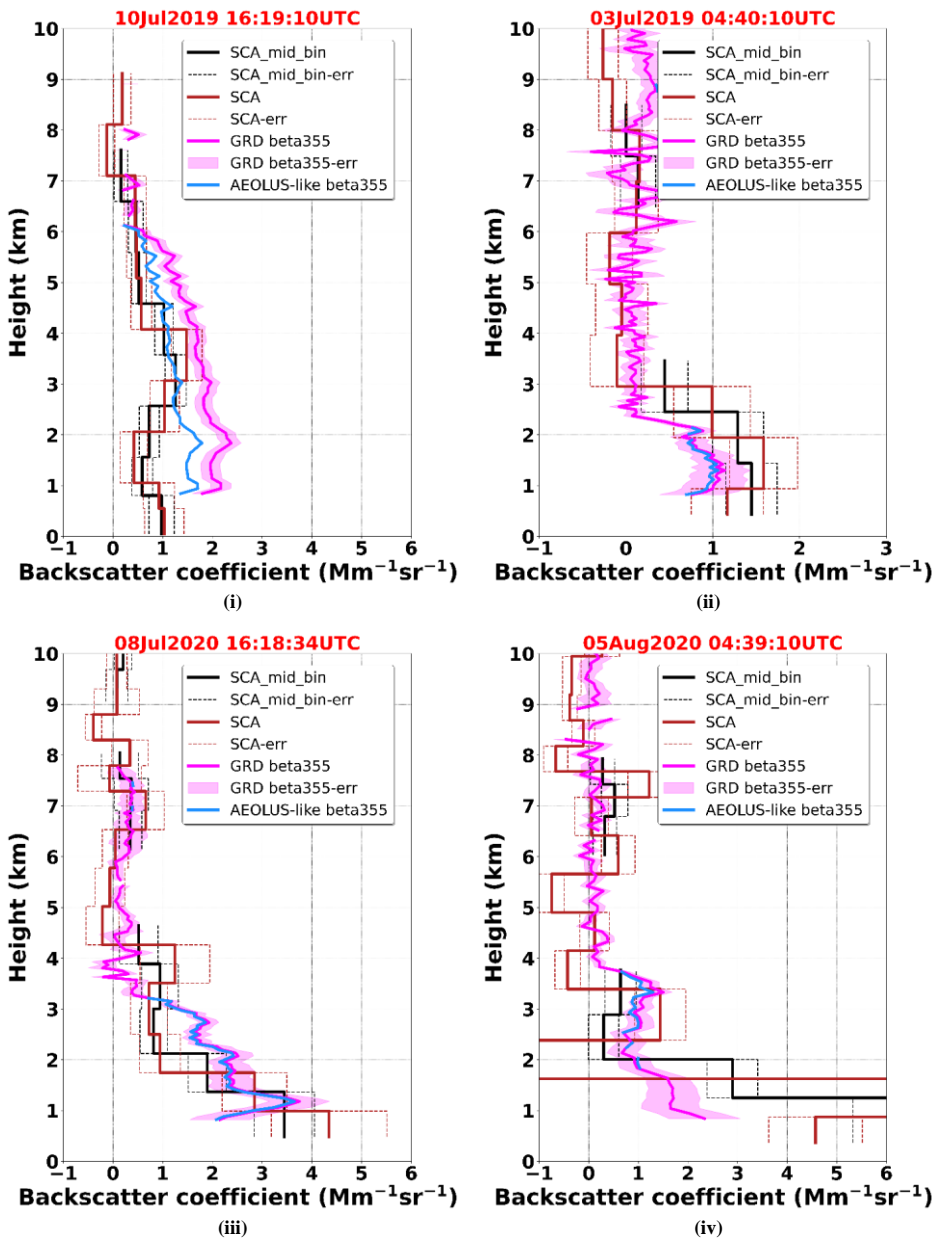
Figure 3: Vertical profiles of backscatter coefficient at 355 nm acquired by ALADIN for the Level 2A SCA (regular vertical observation grid, brown solid curve) and SCA mid-bin (reduced vertical observation grid, black solid curve) products. The dashed lines correspond to the estimated SCA backscatter coefficient errors (brown) and SCA mid-bin backscatter coefficient errors (black). Vertical profile of Polly[XT] backscatter coefficient (pink solid curve) at UV wavelength (355 nm) and associated errors (pink shaded area). Polly[XT] Aeolus-like backscatter coefficient (light-blue

solid curve) after converting the linear-derived products to circular co-polar according to Paschou et al. (2022). The

ground-based profiles have been acquired at the Antikythera station (southwest Greece) on: (i) 10th July 2019, (ii) 3rd July 2019, (iii) 8th July 2020 and (iv) 5th August 2020. The red color font denotes which Aeolus BRC (along with the overpass time) has been selected based on the defined collocation criteria.
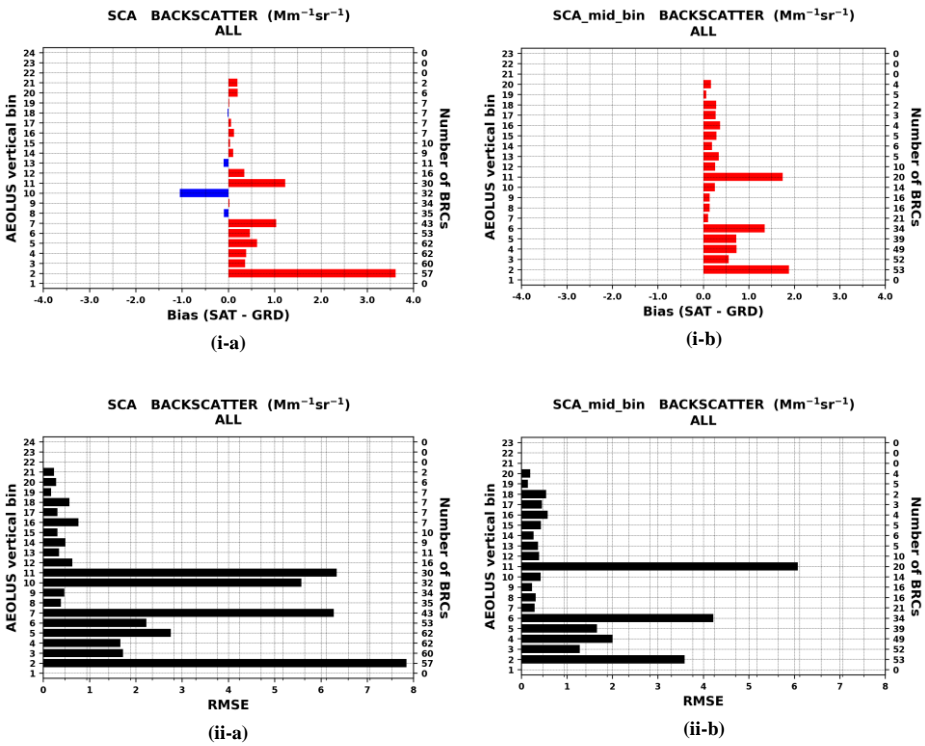
Figure 4: Bias (i) and root mean square error (ii) metrics for the unfiltered Aeolus L2A backscatter retrievals reported at the regular (a) and mid-bin (b) vertical scales. The biases are defined as SAT-GRD and the positive/negative departures are depicted with red/blue bars. The statistical metrics are vertically resolved based on Aeolus bins indices (left y-axis). The number of BRCs participating in the metrics calculations at each bin are given on the right y-axis.
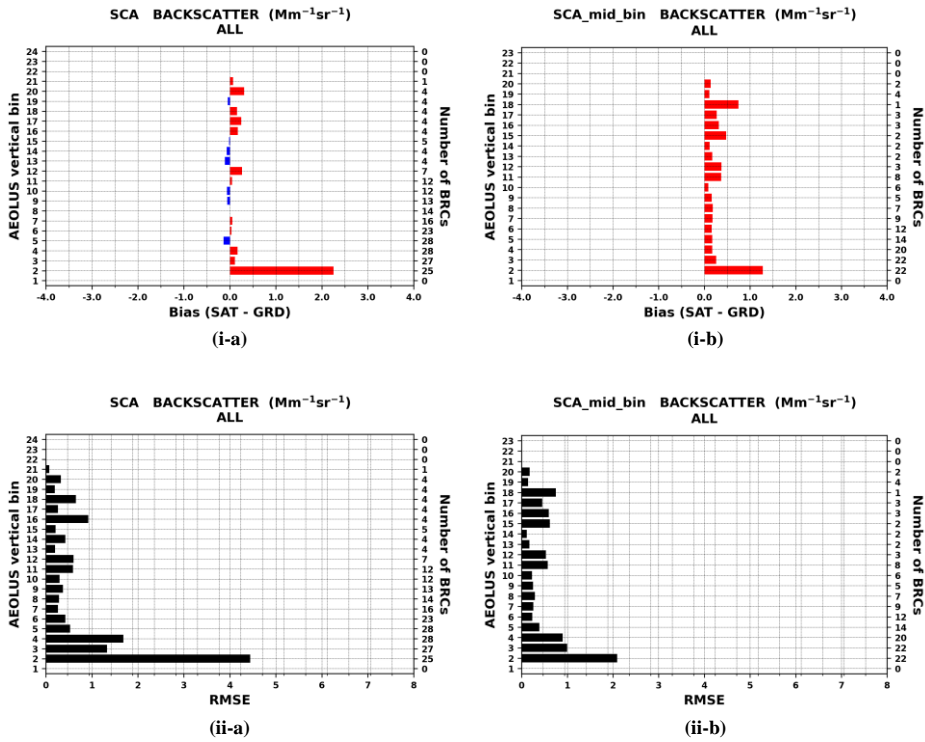
Figure 5: As in Figure 4 but for the filtered Aeolus L2A backscatter retrievals.

1724
1725
1726
1727
1728
1729
1730
1731
1732
1733
1734
1735
1736
1737
1738
1739
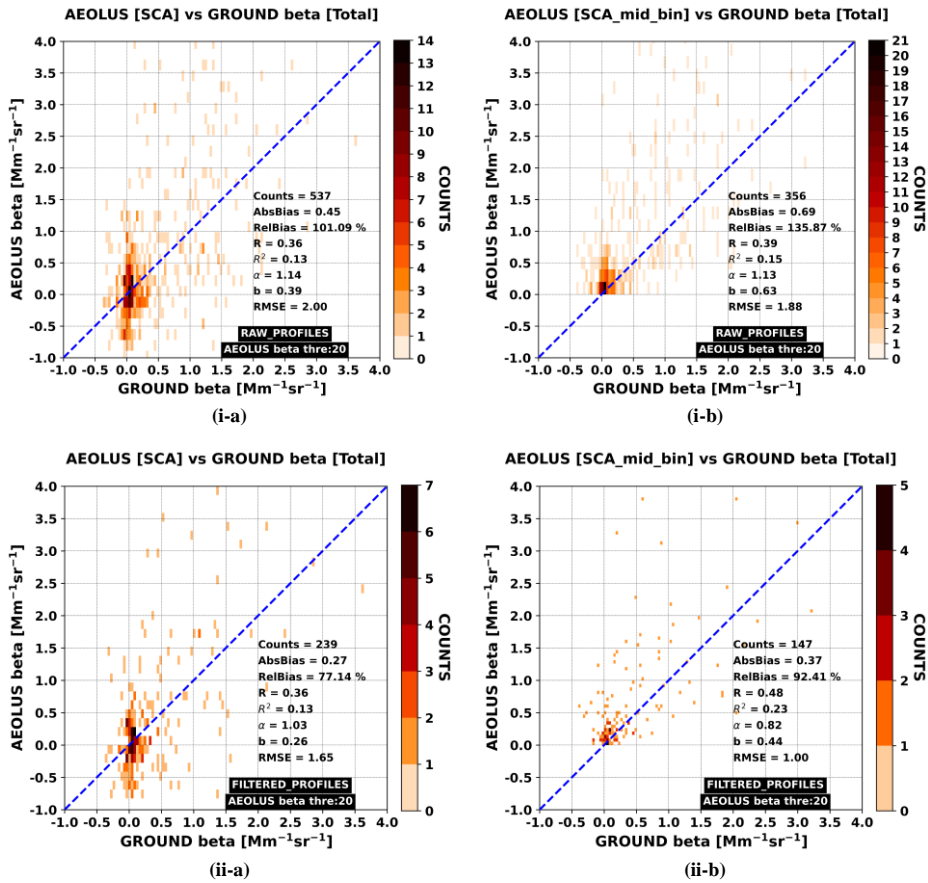
Figure 6: 2D histograms between Aeolus (y-axis) and ground-based (x-axis) backscatter coefficient retrievals. In the upper (i) and bottom (ii) panels are depicted the results for the cloud+aerosol backscatter (unfiltered) and cloud-cleared backscatter (filtered) Aeolus profiles, respectively. On the left and right columns are illustrated the results corresponding to Aeolus regular (24 bins) and mid-bin (23 bins) vertical scales, respectively. Aeolus backscatter values larger than 20 Mm^{-1} sr^{-1} are masked out from the collocated sample.
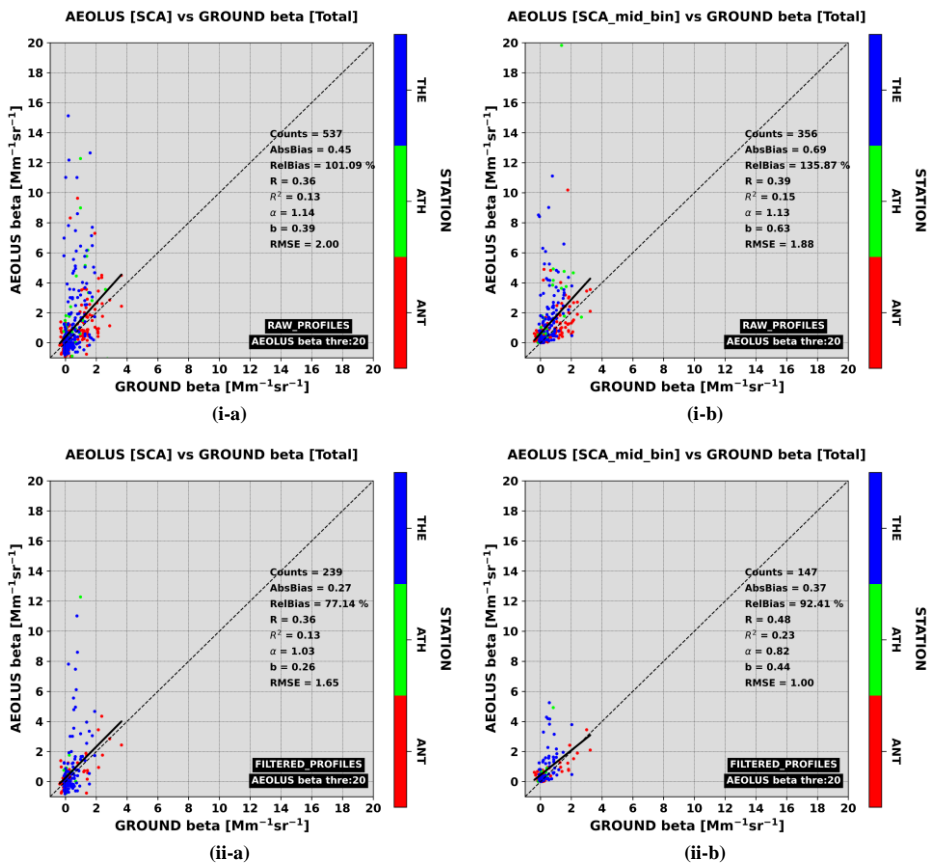
Figure 7: Scatterplots between Aeolus (y-axis) and ground-based (x-axis) backscatter coefficient retrievals resolved based on the indices of Aeolus vertical bins (colored circles). In the upper (i) and bottom (ii) panels are depicted the results for the unfiltered and filtered Aeolus profiles, respectively. On the left and right columns are illustrated the results corresponding to Aeolus regular (24 bins) and mid-bin (23 bins) vertical scales, respectively. Aeolus backscatter values larger than 20 Mm^{-1} sr^{-1} are masked out from the collocated sample.